metals

MDPI

Article

$Mg_2(Co_{1/3}Fe_{1/3}Ni_{1/3})$ Processed by Ball-Milling/Annealing and High-Pressure Torsion for Hydrogen Storage, a Hydriding/Dehydriding Cycling Stability Testing

Karina Suárez-Alcántara [1,*], Nidia Libia Torres-García [1], Paula del Carmen Cintron-Núñez [1,2], Joaquín Eduardo González-Hernández [3], Jorge Mauricio Cubero-Sesin [3], Espiridión Martínez-Aguilar [1] and Rigoberto López-Juárez [1]

[1] Morelia Unit of Materials Institute Research, National Autonomous University of Mexico, Antigua Carretera a Pátzcuaro No. 8701, Col. Ex Hacienda de San José de la Huerta, Morelia CP 58190, Mexico; nidia.torres@iim.unam.mx (N.L.T.-G.); paula.cintron.nunez@cinvestav.mx (P.d.C.C.-N.); espiridionmartinezaguilar@gmail.com (E.M.-A.); rlopez@iim.unam.mx (R.L.-J.)

[2] Nanoscience and Nanotechnology Program, Centro de Investigación y de Estudios Avanzados (CINVESTAV-IPN), Av. Instituto Politécnico Nacional 2508, San Pedro Zacatenco, Gustavo A. Madero, Ciudad de México CP 07360, Mexico

[3] Centro de Investigación y Extensión en Ingeniería de los Materiales (CIEMTEC), Escuela de Ciencia e Ingeniería de los Materiales, Instituto Tecnológico de Costa Rica, Cartago 159-7050, Costa Rica; jegonzalez@itcr.ac.cr (J.E.G.-H.); jcubero@itcr.ac.cr (J.M.C.-S.)

* Correspondence: karina_suarez@materiales.unam.mx

Abstract

A mandatory prerequisite for a good hydrogen storage material is long-term stability in hydriding/dehydriding reactions, in a suitable temperature interval (250–350 °C for magnesium intermetallics). A 50-cycle hydriding/dehydriding stability test of two $Mg_2(Co_{1/3}Fe_{1/3}Ni_{1/3})$ materials is presented. $Mg_2(Co_{1/3}Fe_{1/3}Ni_{1/3})$ was processed progressively by ball milling and annealing, followed by high-pressure torsion. A comparison of the effects of the processing on the cycling test is presented. X-ray diffraction, scanning and transmission electron microscopy, and infrared characterization indicate the morphological and structural changes in the materials after production and cycling. The highest hydrogen storage was 3.55 wt.% and 3.25 wt.% for the ball-milled and annealed $Mg_2(Co_{1/3}Fe_{1/3}Ni_{1/3})$ and high-pressure torsion processed $Mg_2(Co_{1/3}Fe_{1/3}Ni_{1/3})$, respectively, at 15 bar and 300 °C. After 50 cycles of hydriding/dehydriding reactions, the hydriding onset temperature is 69 °C and 50 °C for the ball-milled and annealed $Mg_2(Co_{1/3}Fe_{1/3}Ni_{1/3})$ and high-pressure torsion processed $Mg_2(Co_{1/3}Fe_{1/3}Ni_{1/3})$, respectively. Meanwhile, the dehydriding onset temperatures are 257 °C and 223 °C, with hydrogen storage losses of 16% and 7.4% for the ball-milled and annealed $Mg_2(Co_{1/3}Fe_{1/3}Ni_{1/3})$ and the high-pressure torsion processed $Mg_2(Co_{1/3}Fe_{1/3}Ni_{1/3})$, respectively. Overall, the ball-milled and annealed $Mg_2(Co_{1/3}Fe_{1/3}Ni_{1/3})$ material presented better performance.

Keywords: Hydrogen storage; multi-element Mg-based complex hydrides; high-pressure torsion (HPT); cycling testing

Academic Editor: Félix Echeverría

Received: 13 March 2026
Revised: 12 April 2026
Accepted: 15 April 2026
Published: 17 April 2026

1. Introduction

Research on new solid materials or processing techniques for hydrogen storage is ongoing [1–4]. For hydrogen to be realized as an energy vector [5], it is necessary to overcome the difficulties of hydrogen storage and transportation [6,7]. The main objective is to produce a

suitable material with high hydrogen storage capacity, rapid hydriding and dehydriding kinetics, pressure and temperature operation conditions compatible with other hydrogen technologies, reversible storage upon long-term cycling, low cost, etc. [3,8]. Among the materials for hydrogen storage, Mg-based intermetallics stand out because they combine acceptable hydrogen storage with improved kinetics and thermodynamics provided by alloying elements [9–13]. The notable Mg intermetallics suitable for hydrogen storage are those containing Ni, Co, Fe, or combinations thereof [14–17]. Recently, our research group reported a combinatorial study on $Mg_2(Co_{1/3}Fe_{1/3}Ni_{1/3})$, $Mg_2(Cu_{1/3}Fe_{1/3}Ni_{1/3})$, $Mg_2(Co_{1/3}Cu_{1/3}Fe_{1/3})$, $Mg_2(Co_{1/3}Cu_{1/3}Ni_{1/3})$, and $Mg_2(Co_{1/4}Cu_{1/4}Fe_{1/4}Ni_{1/4})$ produced by ball-milling [18]. The combination of different elements in a Mg matrix demonstrated changes in kinetics and thermodynamics as compared with pure Mg or individual formation of intermetallics such as Mg_2NiH_4, Mg_2CoH_5, or Mg_2FeH_6 [14,16]. In that report [18], the $Mg_2(Co_{1/3}Fe_{1/3}Ni_{1/3})$ material demonstrated promising hydrogen storage properties due to synergistic effects between the alloying components Co, Fe, and Ni.

Severe plastic deformation processes are defined as material-forming techniques that involve ultra-large plastic deformation without significant changes in the overall shape of the specimen [4,19]. These processes are mainly employed to produce ultrafine-grained or nanocrystalline materials [20–22]. Among SPD methods, high-pressure torsion (HPT) is one of the most widely used to optimize the kinetic properties of alloys for hydrogen storage [22–25]. This method consists of applying very high pressure (5–6 GPa) combined with shear strain generated by the torsion of the material between two anvils. As a result, high dislocation densities and extreme grain refinement have been observed in the materials processed by HPT [26–29]. In the context of solid-state hydrogen storage, grain and crystal size reduction combined with an increase in crystal defects is expected to promote hydrogen diffusion and sorption [30]. Several studies have demonstrated that alloys processed by HPT exhibit faster hydrogen absorption and desorption kinetics, higher reversible storage capacity, and lower desorption temperatures compared to their as-cast or annealed counterparts [31–37]. However, the effects of HPT also depend on the chemical composition of the alloy, its processing history (e.g., previous ball milling), and the processing conditions (e.g., applied pressure, number of turns, rotation speed, and temperature). In Mg-based alloys, HPT refines the microstructure to the nanoscale [38,39]. It also improves kinetics and reversibility in the MgH_2–Fe, Mg–Ni, and Mg–Zr systems [33,40]. In Mg–Ni alloys, HPT promotes the formation of nanograins, stacking faults, and microcracks, thereby accelerating hydrogen activation and absorption [34]. In the present work, the HPT process was applied to improve the distribution of the transition metals Co, Fe, and Ni within the Mg matrix, and then, evaluate its effect on the formation of intermetallic mixtures and the hydrogen storage characteristics.

Cycling studies must be conducted to determine material durability, a key parameter, in terms of the number of cycles. The ultimate number proposed by the DOE is 1500 [41]. Unfortunately, many hydrogen storage materials do not support hydriding/dehydriding reactions beyond a few cycles. On the other hand, extensive cycling studies require prolonged use of measurement apparatus, which is often not feasible. As a result, material durability is not reported as frequently as it should be. In the present work, we report a 50-cycle hydriding/dehydriding stability test of $Mg_2(Co_{1/3}Fe_{1/3}Ni_{1/3})$. The physicochemical characterization of the materials after cycling experiments helps to explain the degradation process underlying the reduction in hydrogen uptake.

2. Materials and Methods

2.1. Preparation of Samples

The $Mg_2(Co_{1/3}Fe_{1/3}Ni_{1/3})$ mixture was produced as loose powders and as a consolidated solid material through ball-milling and annealing, and then high-pressure torsion processing. The metals Mg, Co, Fe, and Ni were used as powders, size -325 mesh, from Alfa-Aesar (St. Louis, MO, USA) with a minimum purity of 99.8%. The stoichiometric quantities to mix 2 g of $Mg_2(Co_{1/3}Fe_{1/3}Ni_{1/3})$ were charged into a 50 mL stainless-steel milling vial along with six yttria-stabilized zirconia balls of 1 cm diameter. The ball-to-powder weight ratio was 10:1. Milling was performed in a shaker-type mill (Retsch, Haan, Germany) at room temperature and an agitation rate of 30 Hz. The milling was divided into 40 cycles of 30 min of milling and 10 min of pause, for a total milling time of 20 h. After milling, the mixture was annealed under a vacuum at 350 °C for 6 h. At this stage, a portion of the mixture was characterized and tested for hydrogen storage. Hereafter, this material is referred to as BM-A-$Mg_2(Co_{1/3}Fe_{1/3}Ni_{1/3})$. The remaining portion (1 g) was further processed by HPT, as described below.

The milled and annealed powders were pre-compacted into 10 mm-diameter disks under 2 tons of pressure for 30 min. Each disk weighed 200 mg. Up to this stage, the materials were stored, handled, and prepared under an argon atmosphere in a Vigor® glovebox (with O_2 and H_2O levels below 5 ppm, Houston, TX, USA). The pre-compacted disks were confined in cans filled with high-purity argon and sent to the CIEMTEC in Costa Rica for the HPT processing. From this point onward, the material was handled in air. The HPT process was carried out using custom-built equipment consisting of a 200-ton hydraulic press (YH32-200 XZPRESTEK, SISELEC SA, San José, Costa Rica) [42]. The pre-compacted disks were subjected to 10 turns at 1 rpm (6°/s) under a pressure of 5 GPa (50,000 bar) at room temperature to produce a fully consolidated disk of 10 mm in diameter and about 0.5 mm thick. The material is hereafter referred to as HPT-$Mg_2(Co_{1/3}Fe_{1/3}Ni_{1/3})$. The BM-A-$Mg_2(Co_{1/3}Fe_{1/3}Ni_{1/3})$ and HPT-$Mg_2(Co_{1/3}Fe_{1/3}Ni_{1/3})$ materials were subsequently characterized and tested for hydrogen storage.

2.2. Temperature-Programmed Hydriding and Dehydriding Reactions

Fifty complete cycles of hydriding and dehydriding reactions were performed for both BM-A-$Mg_2(Co_{1/3}Fe_{1/3}Ni_{1/3})$ and HPT-$Mg_2(Co_{1/3}Fe_{1/3}Ni_{1/3})$. The cycling test was conducted using a Sieverts-type apparatus of our design and construction [43]. About 300 mg of each material was used. The BM-A-$Mg_2(Co_{1/3}Fe_{1/3}Ni_{1/3})$ powders were confined in the sample holder of the Sieverts-type apparatus directly from the glovebox, without air exposure. For the consolidated HPT-$Mg_2(Co_{1/3}Fe_{1/3}Ni_{1/3})$ material, about 1.5 disks were crushed with a hammer (no argon atmosphere protection used). The initial disks, 10 mm in diameter, were fragmented into irregular pieces of approximately 3 mm to allow passage through the sample holder nozzle (4 mm in diameter). The pieces were confined in the sample holder of the Sieverts-type reactor [43].

The previous step in the materials cycling test is calibrating the Sieverts-type apparatus. Calibration and operation details were performed as reported elsewhere [43]. In brief, the calibration was performed to determine the void volume (the space not occupied by the sample) in the sample holder. The determination of the void volume is performed by expanding known aliquots of a high-purity gas (Ar or He) under isothermal conditions.

Hydriding and dehydriding reactions were performed through temperature-programmed experiments after setting an initial hydrogen pressure, the details are described below. Hydrogen was introduced into the apparatus at 15 bar and room temperature for hydriding reactions. Then, the sample was heated from room temperature to 300 °C at a heating rate of 5 °C/min. However, to avoid minor thermal effects at the beginning of the reactions,

30 °C was selected as the starting temperature for data processing. The time spent under isothermal conditions ranged from 4 h to 10 min. The reaction time was inversely correlated with the activation level of materials: the first cycles were the longest, and subsequent cycles required less time to reach no change in hydrogen pressure. After each hydriding reaction, the reactor was quickly cooled to room temperature, and the remaining hydrogen was released.

For the dehydriding reactions, hydrogen was initially set at 0.015 bar in the apparatus and then heated to 350 °C at a heating rate of 5 °C/min. The time spent under isothermal conditions decreased as cycling progressed. To ensure complete hydrogen release from the samples after each cycle, the dehydriding reaction was forced by applying dynamic vacuum for 15 min at 350 °C. Then, the sample was cooled to room temperature and was ready for the next hydriding/dehydriding cycle.

In total, fifty-one hydriding and fifty dehydriding reactions were performed. The fifty-first hydriding reaction was performed for physicochemical characterization of the hydrided form of the materials. At this stage, all materials were returned to the glove box to prevent oxidation. The hydrogen used in all experiments was of chromatographic purity.

2.3. Pressure–Composition–Temperature (PCT) Curves

PCT curves were obtained on a Quantachrome ISORB-100 apparatus (Quantachrome Instruments, Boynton Beach, FL, USA). Four different samples were tested. The first two correspond to the as-prepared BM-A-$Mg_2(Co_{1/3}Fe_{1/3}Ni_{1/3})$ and HPT-$Mg_2(Co_{1/3}Fe_{1/3}Ni_{1/3})$ materials. The other two correspond to the materials after the cycling test. Approximately 100–150 mg of each material was transferred into the apparatus. The HPT-$Mg_2(Co_{1/3}Fe_{1/3}Ni_{1/3})$ material was hammered to fragment the disks. This conditioning of the sample was performed in the open air. The other materials were transferred from the glove box without exposure to air. Because the post-cycled samples were in a hydrided state, they were dehydrided by heating at 350 °C under dynamic vacuum for 3 h before PCT testing.

After that, a calibration process was performed to determine the void volume of the sample holder. This was performed by expanding a known amount of ultrahigh-purity helium into the sample holder at isothermal conditions. PCT curves were performed by a progressive increase in aliquots of hydrogen gas at pressures from 0.01 to 15 bar. Then, the hydrogen pressure was progressively decreased from 15 to 0.01 bar under isothermal conditions. Reaching the equilibrium determined the time spent at each point. The reaction equilibrium was assumed when the pressure varied by less than 0.1×10^{-3} bar over 1 h, or for up to 4 h per aliquot. The PCT experiments were performed at several temperatures between 275 °C and 350 °C for the as-prepared HPT-$Mg_2(Co_{1/3}Fe_{1/3}Ni_{1/3})$ and at 300 °C for the remaining materials. The hydrogen used during experiments was of chromatographic purity. After finishing the PCT curves, the materials were forced to complete dehydriding by heating in a vacuum at 350 °C for 180 min. Thus, the materials were characterized in a dehydrided state after PCT testing.

2.4. Physicochemical Characterization

The as-prepared BM-A-$Mg_2(Co_{1/3}Fe_{1/3}Ni_{1/3})$, HPT-$Mg_2(Co_{1/3}Fe_{1/3}Ni_{1/3})$, and cycled hydrided and dehydrided materials were characterized with X-ray diffraction (XRD), scanning electron microscopy (SEM), transmission electron microscopy (TEM), and Fourier-transformed infrared spectroscopy (FTIR). When needed, the published physicochemical characteristics of Mg_2NiH_4, Mg_2CoH_5, and Mg_2FeH_6 were used for comparison [44,45].

The BM-A-$Mg_2(Co_{1/3}Fe_{1/3}Ni_{1/3})$ and cycled powders were compacted into a dedicated sample holder and covered with a polyimide tape to protect them from ambient

oxygen and moisture. The HPT-$Mg_2(Co_{1/3}Fe_{1/3}Ni_{1/3})$ disks, with a rough surface, were polished to achieve a flat surface suitable for X-ray diffraction data collection. XRD characterization was performed in a Bruker D2 Phaser diffractometer (Karlsruhe, Germany), using a Cu source (K_α = 1.540598 Å). The XRD characterization was performed between 15° and 90°, with a step size of 0.02° and a dwell time of 0.7 s per step. Crystalline phase identification was performed using the Crystallography Open Database (COD).

For SEM characterization, one HPT-$Mg_2(Co_{1/3}Fe_{1/3}Ni_{1/3})$ disk was transversely fractured at approximately the midpoint. A piece was mounted in conductive resin (Technovit 5000, Kulzer GmbH, Hanau, Germany), then it was progressively polished to a mirror finish using diamond suspensions of 3.0, 1.0, and 0.5 µm. Powder samples were prepared in an argon-filled glovebox, where they were carefully dispersed onto carbon-coated adhesive tape. The dispersed powder samples were transferred to the SEM chamber using a glove bag to minimize air exposure; however, brief contact with air was unavoidable during loading into the vacuum system. SEM analyses were performed using a JEOL JSM-7600F (JEOL, Tokyo, Japan) field-emission scanning electron microscope equipped with a Schottky-type emitter and an Oxford INCA X-Act EDS detector (Oxford Instruments, Oxfordshire, UK). SEM imaging was performed using secondary-electron (SE), backscattered-electron (BSE), or low-angle backscattered-electron (LABE) detectors, the latter of which enables compositional contrast. Micrographs were acquired at an accelerating voltage of 10 kV. EDS analyses were performed at 15 kV using the Oxford INCA X-Act detector (Oxford Instruments, Oxfordshire, UK) for qualitative and semi-quantitative elemental characterization.

BM-A-$Mg_2(Co_{1/3}Fe_{1/3}Ni_{1/3})$ and HPT-$Mg_2(Co_{1/3}Fe_{1/3}Ni_{1/3})$ cycled (hydrided) materials were analyzed by transmission electron microscopy (TEM). TEM analyses were performed using a JEOL ARM-200F Schottky-type field-emission transmission electron microscope equipped with a spherical aberration (Cs) corrector in STEM mode. The instrument was operated at 200 keV in bright-field (BF), dark-field (DF), or HAADF configurations. Elemental analysis was carried out using an Oxford Aztec TEM EDS system. For sample preparation, a few milligrams of the samples were dispersed in tetrahydrofuran (THF) inside an argon-filled glovebox. The powders and solvent were sealed in small vials to prevent air and water contamination, and then the vials were sonicated for 10 min outside the glovebox. After sonication, the vials were returned to the inert atmosphere, and the resulting suspensions were drop-cast onto copper TEM grids and allowed to dry at room temperature inside the glove box. The prepared grids were transported to the microscope in argon-sealed containers; only a brief exposure to air occurred during loading of the sample holder into the TEM column. TEM imaging was performed in both bright-field and dark-field modes, while high-resolution STEM-HAADF images were acquired to evaluate nanoscale structural and compositional contrast.

Fourier-transformed infrared spectroscopy (FTIR) was performed on a Thermo Scientific Nicolet iS10 FTIR spectrometer (Waltham, MA, USA) using an attenuated total reflectance (ATR) accessory with a diamond crystal. About 2 mg of the cycled (hydrided) BM-A-$Mg_2(Co_{1/3}Fe_{1/3}Ni_{1/3})$ and HPT-$Mg_2(Co_{1/3}Fe_{1/3}Ni_{1/3})$ powders were mixed with 50 mg of dry KBr in an agate mortar and compacted in a dedicated press; all steps were performed inside the glovebox. However, the materials were briefly exposed to air during data collection. The presented spectra are the average of 32 scans collected for each sample between 650 cm^{-1} and 4200 cm^{-1} at a spectral resolution of 1 cm^{-1}.

2.5. Infrared Calculations by First Principles

First-principles calculations were performed using the Quantum Espresso package (Version 6.8) [46–48]. For the elements Mg, Ni, Co, Fe, and H, optimized norm-conserving

pseudopotentials (ONCPP) were constructed using the open-source pseudopotential interface and unification module (OPIUM) [49,50]. For the exchange-correlation approximation, the PBE (Perdew-Burke-Ernzerhof) functional [51] was used. The plane wave expansion was truncated at a cutoff energy of 1088.5 eV. System optimization was achieved when the magnitude of the residual energy and the force acting on each atom was less than 10^{-5} Ry/atom and 10^{-3} Ry/au, respectively. Brillouin zone sampling was performed using Monkhorst-Pack meshes [52] adapted to each system: a 5 × 5 × 5 mesh for the monoclinic structure of Mg_2NiH_4, a 5 × 5 × 4 mesh for the tetragonal structure of Mg_2CoH_5 [53], and a 5 × 5 × 5 mesh for the cubic structure of Mg_2FeH_6. Phonon frequencies at the center of the Brillouin zone (Γ) were calculated using Density Functional Perturbation Theory (DFPT) [52] implemented in the ph.x module of Quantum Espresso. Infrared activities were obtained from the calculation of the dielectric tensor and Born effective charges [54]. Vibrational spectra were generated by convolution with Lorentzian line shape functions of width 10 cm^{-1}, a value consistent with typical experimental resolutions in vibrational spectroscopy of metal hydrides [54]. The Lorentzian function was defined in Equation (1):

$$L(\nu; \nu_0, I_0, \gamma) = \frac{I_0 \cdot \gamma^2}{(\nu - \nu_0)^2 + \gamma^2} \quad (1)$$

where ν is spectral frequency [cm^{-1}], ν_0 is vibrational mode frequency [cm^{-1}], I_0 is the infrared intensity of the mode, and γ is the full width at half maximum (FWHM) [cm^{-1}].

3. Results

Hydrogen Storage Performance

Figure 1 presents the first, second, and third cycles of hydriding and dehydriding reactions at the BM-A-$Mg_2(Co_{1/3}Fe_{1/3}Ni_{1/3})$ and HPT-$Mg_2(Co_{1/3}Fe_{1/3}Ni_{1/3})$. The complete set of fifty cycles for both materials can be consulted in the Supplementary File, Figures S1–S5. The maximum hydrogen uptake of the material $Mg_2(Co_{1/3}Fe_{1/3}Ni_{1/3})$ is 4.4 wt.% if a stochiometric mixture of $1/3Mg_2NiH_4$ + $1/3Mg_2CoH_5$ + $1/3Mg_2FeH_6$ is formed. Figure 1a presents the record of the first, second, and third hydriding reactions of the BM-A-$Mg_2(Co_{1/3}Fe_{1/3}Ni_{1/3})$ and HPT-$Mg_2(Co_{1/3}Fe_{1/3}Ni_{1/3})$. The ball-milled and annealed (BM-A) material demonstrated an easy reaction with hydrogen, even during the first hydriding, upon reaching the isothermal hydriding temperature of 300 °C. The following hydriding reactions are quick and start at a low temperature, reaching + 0.1 wt.% at 52 °C in the third hydriding reaction. We use the temperature at which the hydriding/dehydriding reaches ±0.1 wt.% as the onset temperature in temperature-programmed reactions. The hydrogen uptake of the BM-A-$Mg_2(Co_{1/3}Fe_{1/3}Ni_{1/3})$ at the third cycle is 3.4 wt.%. Meanwhile, the activation process in the HPT material is slow. The HPT disks were highly compacted; perhaps, the applied pressure for our particular material is too high, and other HPT conditions must be tested. The first hydriding reaction lasted about 420 min without reaching an acceptable hydrogen storage capacity. The second and third hydridings on HPT-$Mg_2(Co_{1/3}Fe_{1/3}Ni_{1/3})$ materials improved the onset temperature: the material reached 0.1 wt.% at 59 °C in the third hydriding reaction. Meanwhile, the hydrogen uptake of the HPT-$Mg_2(Co_{1/3}Fe_{1/3}Ni_{1/3})$ at the third cycle was 2.8 wt.%. This is an improvement over the first cycle, but it is still below expectations.

Figure 1b presents the records of the first, second, and third dehydriding reactions of the BM-A-$Mg_2(Co_{1/3}Fe_{1/3}Ni_{1/3})$ and HPT-$Mg_2(Co_{1/3}Fe_{1/3}Ni_{1/3})$. Figure 1b also illustrates the difficulty of performing dehydriding reactions in consolidated materials. Activation both lowers the onset of dehydriding temperature and improves hydrogen release values. The onset dehydriding temperature at the third cycle is 230 °C for HPT-

$Mg_2(Co_{1/3}Fe_{1/3}Ni_{1/3})$ and 259 °C for BM-A-$Mg_2(Co_{1/3}Fe_{1/3}Ni_{1/3})$ material. Thus, the HPT-processed material showed a slight advantage in dehydriding temperature compared with the ball-milled and annealed material. Dehydriding reactions are completed at about 340 °C in the third cycle in both materials. Hydrogen release values at the third cycle are 2.9 wt.% and 3.5 wt.% for HPT-$Mg_2(Co_{1/3}Fe_{1/3}Ni_{1/3})$ and BM-A-$Mg_2(Co_{1/3}Fe_{1/3}Ni_{1/3})$, respectively. These values indicate a small amount of hydrogen sorption during cooling in a hydrogen atmosphere after the hydriding reaction for the BM-A-$Mg_2(Co_{1/3}Fe_{1/3}Ni_{1/3})$ and the need for a brief time in a dynamic vacuum to release the residual hydrogen from the previous hydriding reaction for the HPT-$Mg_2(Co_{1/3}Fe_{1/3}Ni_{1/3})$ material.

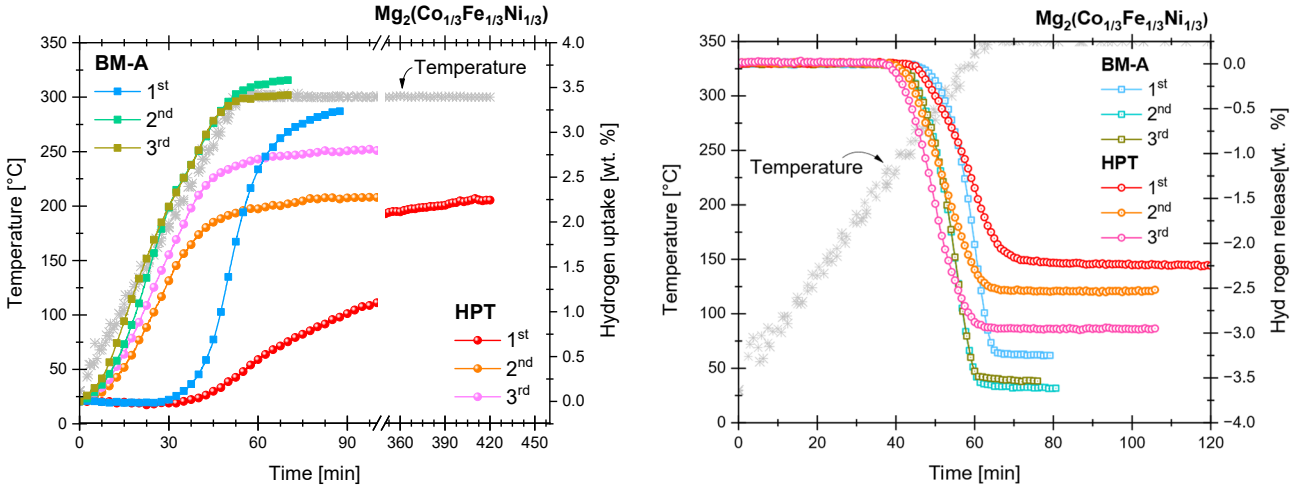

(**a**) (**b**)

Figure 1. First, second, and third cycles of (**a**) hydriding at 15 bar and (**b**) dehydriding at 0.015 bar reactions at the BM-A-$Mg_2(Co_{1/3}Fe_{1/3}Ni_{1/3})$ and HPT-$Mg_2(Co_{1/3}Fe_{1/3}Ni_{1/3})$.

Figure S5 of the Supplementary File groups the record of the tenth, twenty-fifth, and fiftieth hydriding reactions of the BM-A-$Mg_2(Co_{1/3}Fe_{1/3}Ni_{1/3})$ and HPT-$Mg_2(Co_{1/3}Fe_{1/3}Ni_{1/3})$. It took about 10 cycles to reach an almost constant hydrogen uptake in the HPT material (as shown in detail in Figure 2). In contrast, the BM-A-$Mg_2(Co_{1/3}Fe_{1/3}Ni_{1/3})$ material was fully activated at the second cycle. Cycling (Figures S1–S5) induced a small improvement in the hydriding reaction onset temperature in the HPT material. The hydriding onset temperatures are 50 °C for the HPT material and 69 °C for the BM-A material at the 50th cycle. The hydriding reaction evolved from a one-step reaction to a two-step reaction (two slope changes in the hydriding curves) upon cycling. The first step is the formation of MgH_2 [18,55], which was completed at about 200 °C for the HPT material and about 250 °C for the BM-A-$Mg_2(Co_{1/3}Fe_{1/3}Ni_{1/3})$ mixture. Meanwhile, the second hydriding reaction involves the reaction of MgH_2 with transition metals (Co, Fe, and Ni) and hydrogen to form hydrided intermetallics [18].

Figure S5 of the Supplementary File also groups the record of the tenth, twenty-fifth, and fiftieth dehydriding reactions of the BM-A-$Mg_2(Co_{1/3}Fe_{1/3}Ni_{1/3})$ and HPT-$Mg_2(Co_{1/3}Fe_{1/3}Ni_{1/3})$. The dehydriding reactions are clearly grouped by the HPT and BM-A materials. In the HPT material, there is a small advantage in the dehydriding onset temperature: at 223 °C, the HPT material reached −0.1 wt.% in the 50th cycle. The corresponding temperature for the BM-A material is 257 °C. However, hydrogen release is incomplete in the HPT material, necessitating a period under dynamic vacuum to complete the reaction. Finally, the dehydriding reactions (Supplementary File Figures S1–S5) demonstrated a single dehydriding step. This indicated that, under dehydriding conditions, the

decomposition of the intermetallic hydrides and the formation of MgH_2 are close enough to be observed as a single dehydriding step.

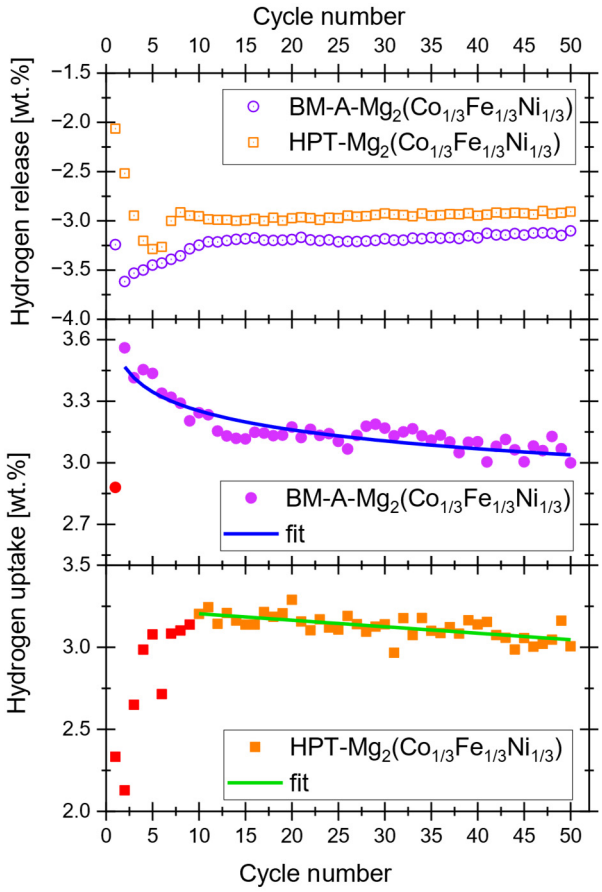

Figure 2. Maximum hydrogen uptake (lower and medium frames) and release (upper frame) as a function of cycle number for BM-A-$Mg_2(Co_{1/3}Fe_{1/3}Ni_{1/3})$ and HPT-$Mg_2(Co_{1/3}Fe_{1/3}Ni_{1/3})$ materials. The red marks, round or square, indicate the excluded points for the fitting of the maximum hydrogen uptake versus the number of cycles. Full marks for hydridings and marks with a small dot for dehydridings. Lines: best fits of hydriding data.

Figure 2 shows the maximum hydrogen uptake and release during cycling for BM-A-$Mg_2(Co_{1/3}Fe_{1/3}Ni_{1/3})$ and HPT-$Mg_2(Co_{1/3}Fe_{1/3}Ni_{1/3})$ materials. The lower frame of Figure 2 presents the maximum hydrogen uptake of HPT-$Mg_2(Co_{1/3}Fe_{1/3}Ni_{1/3})$. Meanwhile, the medium frame shows the BM-A-$Mg_2(Co_{1/3}Fe_{1/3}Ni_{1/3})$ maximum hydrogen uptake. For the hydridings, the maximum hydrogen uptake was achieved at approximately 60 min. That time includes heating from room temperature to 300 °C and approximately 15 min in isothermal conditions. The lower frame of Figure 2 indicates the need for about 10 cycles to reach the maximum hydrogen uptake (full squares) for the HPT-$Mg_2(Co_{1/3}Fe_{1/3}Ni_{1/3})$ material. Meanwhile, the BM-A-$Mg_2(Co_{1/3}Fe_{1/3}Ni_{1/3})$ (full circles) was easily activated. This is related to the reduced available surface area of the HPT-$Mg_2(Co_{1/3}Fe_{1/3}Ni_{1/3})$ material and the progressive crumbling of the consolidated material. Hydrogen uptake stabilized around the tenth cycle (3.25 wt.%) in the HPT-$Mg_2(Co_{1/3}Fe_{1/3}Ni_{1/3})$ material. Subsequently, a slight loss of storage capacity was observed. At the 50th cycle, hydrogen uptake was 3.0 wt.%; this corresponds to a 7.4% loss in hydrogen storage capacity. The light-green line in the lower frame of Figure 2 indicates a linear fit of the maximum hydrogen storage versus the cycle number after full activation

at cycle 10. The fitting for the maximum hydrogen uptake ($H_{2\,Max-up}^{HPT}$) as a function of the cycle number (cn) is

$$H_{2\,Max-up}^{HPT} = 3.24399 - 0.00396 \times cn, \quad R^2 = 0.44 \tag{2}$$

If the tendency indicated by the 10–50 cycles continues, the HPT-$Mg_2(Co_{1/3}Fe_{1/3}Ni_{1/3})$ material would store 2.84 wt.% at the 100th cycle, and the material would completely lose the hydrogen storage capacity at the 819th cycle.

For the BM-A-$Mg_2(Co_{1/3}Fe_{1/3}Ni_{1/3})$ material, full activation is reached in the second cycle. It is said that the material is fully activated when reaching its maximum hydrogen uptake. Ideally, the maximum hydrogen uptake would be the total hydrogen storage capacity. However, several factors reduced hydrogen uptake, including the surface state. Activation is well known to modify the surface state by means of reduction in some oxidized species (minor) or exposition of fresh (non-oxidized) surfaces by means of particle fragmentation (major). The activation process is rather slow; in our experience with Mg materials, it takes at least three cycles, usually more. Thus, achieving a good hydrogen uptake from the second cycle is a good indicator of hydrogen storage performance. In contrast to the HPT material, the BM-A-$Mg_2(Co_{1/3}Fe_{1/3}Ni_{1/3})$ material experienced a rapid decrease in the maximum hydrogen storage from cycle 2 (3.55 wt.%) to cycle 15 (3.11 wt.%). This represents a 12% loss of hydrogen storage capacity. Then the decrease in maximum hydrogen storage capacity becomes slower. At the 50th cycle, the maximum hydrogen storage capacity reached 2.99 wt.%. This corresponds to an accumulated loss of hydrogen storage of almost 16%. The fitting for the maximum hydrogen uptake ($H_{2\,Max-up}^{BM-A}$) as a function of the cycle number (cn) after full activation at the cycle number 2 is

$$H_{2\,Max-up}^{BM-A} = 3.5652 - 0.13319 \times \ln(cn), \quad R^2 = 0.82 \tag{3}$$

If the tendency indicated by the 2–50 cycles continues, the BM-A-$Mg_2(Co_{1/3}Fe_{1/3}Ni_{1/3})$ material would store 2.95 wt.% at the 100th cycle. The predicted hydrogen uptake after 1000 cycles would be 2.64 wt.%. Due to the mathematical form of the fit for the BM-A-$Mg_2(Co_{1/3}Fe_{1/3}Ni_{1/3})$ material, it would take a large number of cycles before complete deactivation.

The upper frame of Figure 2 presents the maximum hydrogen release for both tested materials. The reported values reveal the dependency of hydrogen release on hydrogen uptake and activation. The collected data indicate, in general, a good hydrogen release. Hydrogen release is better in the BM-A-$Mg_2(Co_{1/3}Fe_{1/3}Ni_{1/3})$ material. Meanwhile, in the HPT-$Mg_2(Co_{1/3}Fe_{1/3}Ni_{1/3})$ material, it is necessary to apply dynamic vacuum to release all previously stored hydrogen.

The PCT curves can be consulted in Supplementary File Figure S6. PCT curves reflect changes in equilibrium pressure as a function of the processing history of $Mg_2(Co_{1/3}Fe_{1/3}Ni_{1/3})$. The as-prepared BM-A-$Mg_2(Co_{1/3}Fe_{1/3}Ni_{1/3})$ achieved 3.8 wt.% and equilibrium pressures of 0.55 and 2.3 bar for the two successive hydridings, i.e., the formation of MgH_2 in the first step and then the formation of the intermetallic hydrides. Meanwhile, the HPT-$Mg_2(Co_{1/3}Fe_{1/3}Ni_{1/3})$ "freshly fractured" exhibited a lower hydrogen uptake of 2.7 wt.%. The hydriding equilibrium pressures are 0.38 and 2.3 bar for the formation of MgH_2 in the first step, followed by the formation of intermetallic hydrides. It is interesting that the formation of MgH_2 equilibrium pressure (0.38 bar) is lower than the expected equilibrium pressure for pure MgH_2 (0.7 bar, dotted line in the PCT diagrams of the present work). This can be a collective effect of the presence of Co, Ni, and Fe that can catalyze the hydriding reaction and the microstructural changes induced by the HPT process. The Figure S6 in the Supplementary File also presents a set of PCT curves of HPT-

$Mg_2(Co_{1/3}Fe_{1/3}Ni_{1/3})$ "freshly fractured". Interestingly, the HPT-$Mg_2(Co_{1/3}Fe_{1/3}Ni_{1/3})$ "freshly fractured" material presented a partial reversibility even at 275 °C (Figure S6). However, it is evident that the low hydrogen storage capacity is due to the low exposed area of the consolidated materials.

For its part, the PCT curve of BM-A-$Mg_2(Co_{1/3}Fe_{1/3}Ni_{1/3})$ after cycling demonstrated an almost full hydrogen uptake capacity (4.4 wt.%). This is the result of prolonged heating in a vacuum prior to PCT, which could reactivate the material after cycling. However, the after cycling PCT curve of BM-A-$Mg_2(Co_{1/3}Fe_{1/3}Ni_{1/3})$ presented an increased hysteresis between the hydriding and dehydriding branches of the PCT curves as compared to the as-prepared materials. The equilibrium pressures are 2.6 bar and 4.2 bar for the two hydriding steps. HPT-$Mg_2(Co_{1/3}Fe_{1/3}Ni_{1/3})$ material after cycling demonstrated a hydrogen uptake of 3.4 wt.%. That value is similar to the hydriding achieved in the fully activated cycling test. This also indicated a reactivation after the cycling test. However, the hydriding equilibrium pressures changed to 1.4 and 9 bar, for the first and second steps of hydriding, respectively. As in the BM-A material, an increase in hysteresis between hydriding and dehydriding reactions is observed. Regarding the dehydriding equilibrium pressures, the PCT curves indicated that the HPT materials exhibited lower equilibrium pressures for H_2 release than the BM-A materials. Additionally, the dehydriding process is incomplete at 300 °C in the cycled material. Thus, the material history is essential; processing and cycling induce changes in the material.

Figure 3 presents the X-ray diffraction characterization of the BM-A-$Mg_2(Co_{1/3}Fe_{1/3}Ni_{1/3})$ and HPT-$Mg_2(Co_{1/3}Fe_{1/3}Ni_{1/3})$. The X-ray diffraction pattern of the ball-milled powders of $Mg_2(Co_{1/3}Fe_{1/3}Ni_{1/3})$ is composed of the respective peaks of Mg, Co, Fe, and Ni, without indications of Mg-intermetallics [18]. The annealing of ball-milled $Mg_2(Co_{1/3}Fe_{1/3}Ni_{1/3})$, included in the lower frame of Figure 3, demonstrated the formation of the intermetallic Mg_2Ni. Additionally, the BM-A-$Mg_2(Co_{1/3}Fe_{1/3}Ni_{1/3})$ presents a prominent peak at about 44.7°, which includes contributions of the main peaks of Fe (body-centered cubic (110)), Ni (face-centered cubic (111)), and a secondary peak of Co (hexagonal (002)). Fe is, in practical terms, not soluble in Mg [56]. Thus, Fe integration in the Mg matrix is difficult, and its diffraction peaks are prominent. Additionally, the peak at 44.7° shows a secondary peak at 45.09° (inset in the lower frame of Figure 3) that is identified as the main peak of Mg_2Ni. A small shift to lower diffraction angles was observed in the Mg_2Ni peaks. This can indicate the dissolution of Fe or Co in the Mg_2Ni phase during annealing at 350 °C for 6 h.

The peak at 44.7° in the HPT-$Mg_2(Co_{1/3}Fe_{1/3}Ni_{1/3})$ material still shows the main Fe contribution. The same peak might indicate the presence of Ni. However, due to the lack of additional Ni peaks, Ni dissolution in the Mg matrix and partial formation of Mg_2Ni are expected. The peak intensity of the Mg_2Ni is evident in the HPT-$Mg_2(Co_{1/3}Fe_{1/3}Ni_{1/3})$ material. The broad peaks indicate nanoparticle formation. Another effect observed after HPT is a decrease in Co peak intensity; this may be due to partial distribution of Co in the Mg matrix. Additionally, HPT processing decreased the relative peak intensity of Mg and produced texture; the Mg (002) peak is more intense than expected, whereas the Mg (101) peak is less intense than expected. Other expected Mg peaks of low intensity decreased to the noise level after the HPT. The formed Mg_2Ni also shows texture; the principal peak would be located at 45.21° (45.09° observed) and corresponds to the (203) plane. However, the main peak of the Mg_2Ni in the HPT-processed material is located at 20.08° (expected at 20.15°) and corresponds to the (003) plane. The small shift toward lower diffraction angles, observed in the Mg_2Ni peaks after annealing, was maintained after HPT. Compared to the diffraction peaks of Mg and Mg_2Ni, the XRD peaks broadened after HPT processing, indicating that the crystallite size is smaller than in the annealed state.

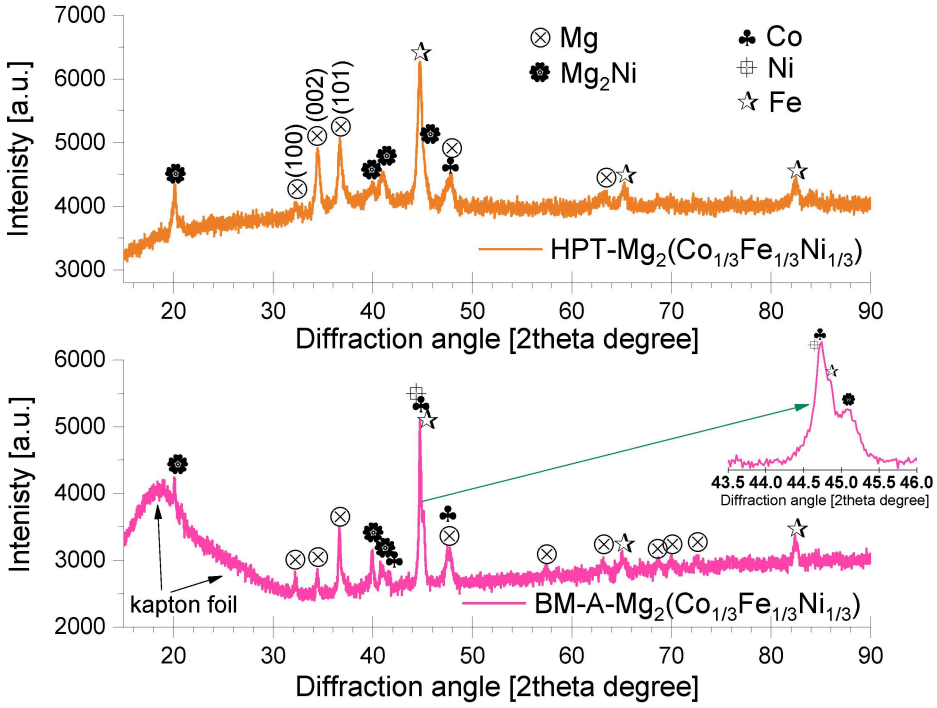

Figure 3. X-ray diffraction of the BM-A-$Mg_2(Co_{1/3}Fe_{1/3}Ni_{1/3})$ (lower frame) and HPT-$Mg_2(Co_{1/3}Fe_{1/3}Ni_{1/3})$ (upper frame). The references for crystallographic data are: Mg COD-9008506, Co COD-9008492, Fe COD-9008536, Ni COD-9008476, and Mg_2Ni COD-1522843. The green arrow indicates a zoom of the main peak.

Figure 4 presents the XRD characterization after the cycling test in the hydrided stage. The lower frame of Figure 4 presents X-ray diffraction of the cycled and hydrided HPT-$Mg_2(Co_{1/3}Fe_{1/3}Ni_{1/3})$. The main phases are MgH_2, monoclinic Mg_2NiH_4, cubic Mg_2NiH_4, and Mg_2FeH_6. The main peaks of the monoclinic Mg_2NiH_4, cubic Mg_2NiH_4, and cubic Mg_2FeH_6 present coincidences with diffraction peaks observed at 23.7° and between 38 and 43 Mg_2CoH_5 peaks were not detected, nor were Co peaks; thus, a dilution of the Co and Co-intermetallics in the alloy matrix is anticipated [15]. Additionally, the presence of Fe can be observed. This corroborates the incomplete hydriding reactions and the need for higher hydrogen pressure or temperature. The X-ray diffraction of the cycled and hydrided BM-A-$Mg_2(Co_{1/3}Fe_{1/3}Ni_{1/3})$ is presented in the upper frame of Figure 4. The XRD of the BM-A-$Mg_2(Co_{1/3}Fe_{1/3}Ni_{1/3})$ and the HPT-$Mg_2(Co_{1/3}Fe_{1/3}Ni_{1/3})$ are quite similar; however, the main difference is a higher relative peak intensity of the monoclinic Mg_2NiH_4 in the hydrided BM-A-$Mg_2(Co_{1/3}Fe_{1/3}Ni_{1/3})$ as compared to the hydrided HPT-$Mg_2(Co_{1/3}Fe_{1/3}Ni_{1/3})$.

The XRD of the dehydrided form of HPT-$Mg_2(Co_{1/3}Fe_{1/3}Ni_{1/3})$ and BM-A-$Mg_2(Co_{1/3}Fe_{1/3}Ni_{1/3})$ after cycling is presented in the upper frame of Figure 5. The main characteristics are the presence of Mg, Mg_2Ni, and Fe. In Mg, the texture (observed in the as-prepared HPT-processed material in Figure 3) was completely eliminated. Also, by comparing the relative intensities of the Mg peaks to the Kapton foil peak, the Mg peak intensity is reduced in the cycled and dehydrided HPT-$Mg_2(Co_{1/3}Fe_{1/3}Ni_{1/3})$ material. This can be related to the formation of Mg_2Ni, whose peaks are more intense than in the BM-A material. Additionally, the Mg_2Ni peaks are shifted by about 0.15° to lower diffraction angles; partial substitution of Ni by Co or Fe may account for the slight shift. In both materials, no peaks of Ni were located; meanwhile, the main peak of Fe is evident at 44.67°. The wide peak located at 47.47° corresponds to Mg, but also can contain the main peak of hexagonal Co. No clear indication of the formation of Mg-Co intermetallics was obtained [57]. Interestingly, an intense peak at 29.3° emerged after cycling in the dehydrided form of the

HPT-$Mg_2(Co_{1/3}Fe_{1/3}Ni_{1/3})$ material. This peak is marked as unidentified; no match with the reported intermetallics of Mg or alloys of Co, Fe, or Ni was obtained. Finally, and contrary to expectations, the peak heights and widths after cycling exhibit characteristics typical of nanocrystalline materials. The expectation following continuous heating and cooling in a hydrogen/vacuum atmosphere was the nucleation and growth of crystals to a considerable size.

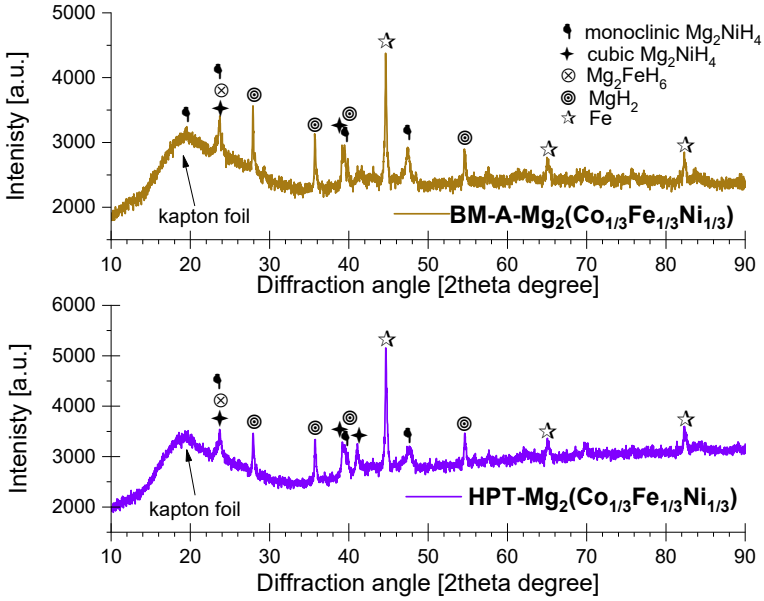

Figure 4. X-ray diffraction of cycled and hydrided HPT-$Mg_2(Co_{1/3}Fe_{1/3}Ni_{1/3})$ (**lower frame**) and cycled and hydrided BM-A-$Mg_2(Co_{1/3}Fe_{1/3}Ni_{1/3})$ (**upper frame**). The references for crystallographic data are: MgH_2-COD 4124639, cubic-Mg_2NiH_4 COD-1521145, monoclinic-Mg_2NiH_4 COD-1524991, Mg_2CoH_5, adapted from Ref. [58], and Mg_2FeH_6, adapted from Refs. [59,60].

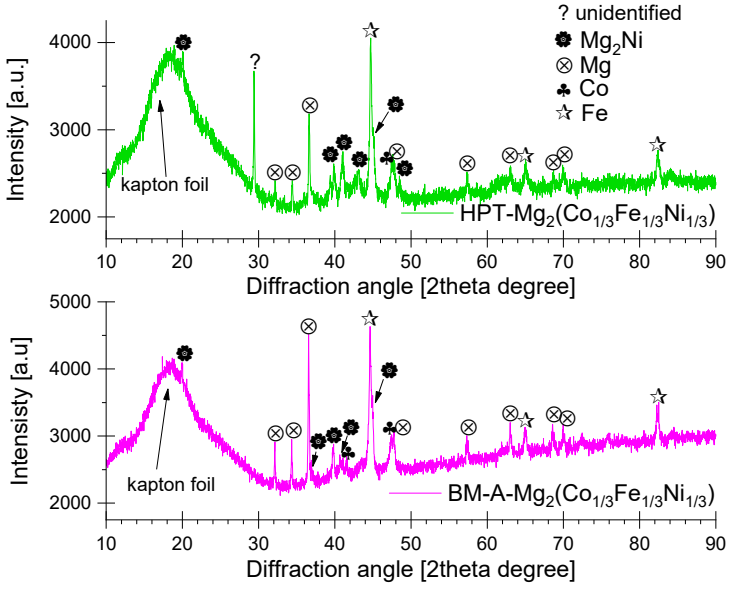

Figure 5. X-ray diffraction of cycled HPT-$Mg_2(Co_{1/3}Fe_{1/3}Ni_{1/3})$ and BM-A-$Mg_2(Co_{1/3}Fe_{1/3}Ni_{1/3})$ in the dehydrided form. The references of crystallographic data were: Mg COD-9008506, Co COD-9008492, Fe COD-9008536, and Mg_2Ni COD-1522843.

Figure 6 presents SEM and elemental mapping images of the BM-A-$Mg_2(Co_{1/3}Fe_{1/3}Ni_{1/3})$. The corresponding SEM images of the as-milled material are available elsewhere [18]. The BM-A-$Mg_2(Co_{1/3}Fe_{1/3}Ni_{1/3})$ material exhibits globular agglomerates with diameters

between 10 and 250 µm. From Figure 6 and the report of ref. [18], we can conclude that the annealing process was very limited in changing the morphology and size of particles as compared with as-milled materials. However, annealing significantly improved the homogeneous distribution of Ni in the BM-A-$Mg_2(Co_{1/3}Fe_{1/3}Ni_{1/3})$ material. In contrast, the distribution of Co improved to a small degree, while the homogeneous distribution of Fe did not improve. Distinctive Fe-rich zones are evident in the elemental mapping images in Figure 6. This is an effect of the low solubility of the Fe in Mg.

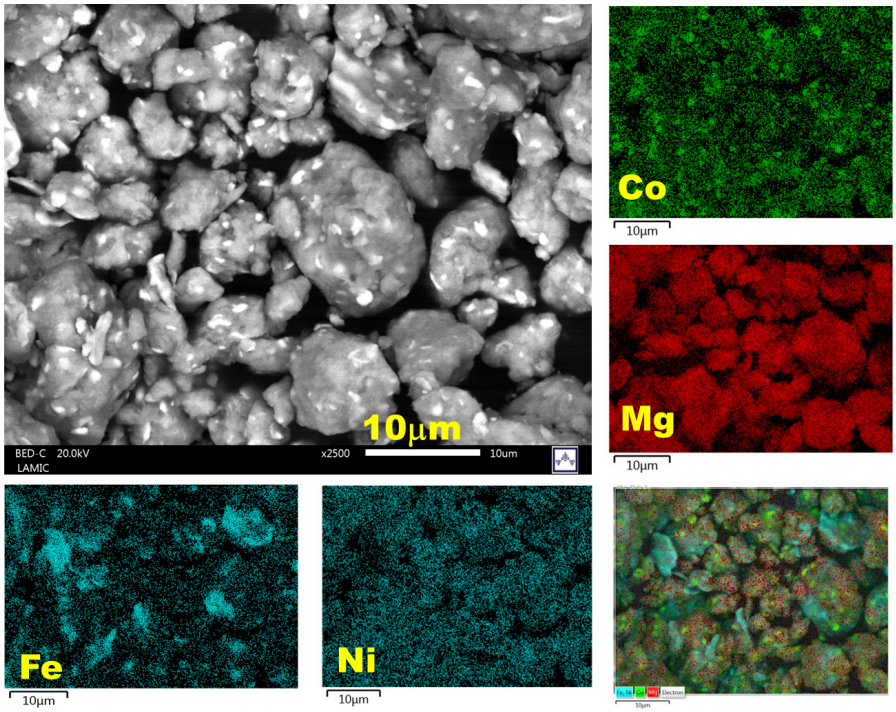

Figure 6. SEM image and elemental mappings of BM-A-$Mg_2(Co_{1/3}Fe_{1/3}Ni_{1/3})$.

Figure 7 presents a set of SEM images of HPT-$Mg_2(Co_{1/3}Fe_{1/3}Ni_{1/3})$ in a transversal section. The first feature to discuss is the absence of pores in the consolidated material. This has repercussions on reducing the active area and hydrogen diffusion, leading to the low hydrogen uptake values observed in the first cycles of hydriding/dehydriding reactions. Figure 7a presents a section from approximately the center of the disk (lower section of the SEM image) to one edge of the disk (upper section of the SEM image). Figure 7a shows a better homogeneity at the edge of the disk than at the center of the disk. Thus, a microstructural gradient was formed along the radius: while the center exhibits a less deformed region (with a coarser and more heterogeneous structure), toward the edge, a more intense deformation is evident due to the higher shear stress induced by the HPT process. The bright zones indicate the presence of Fe and Co, and the gray zones indicate the preferential presence of Mg. Figure 7b shows an enlarged region near the center of the disk (yellow rectangle), where the accumulated plastic strain is relatively low. Elongated substructures and microcracks can still be distinguished, suggesting heterogeneous deformation and the onset of grain fragmentation. These regions reflect partial or incipient recrystallization resulting from the internal energy generated by the applied shear stress. In turn, the zone delimited by the yellow oval was zoomed, revealing two distinct zones with different microstructures. In the most heterogeneous zone (Figure 7c), the elemental mapping demonstrated an elongation in the radial axis (bottom to top in Figure 7c) of the elements with stronger contrasts, i.e., Fe and Co. In the most homogeneous zone (Figure 7d), the elemental mapping showed a reduction in the particle sizes of Fe and Co.

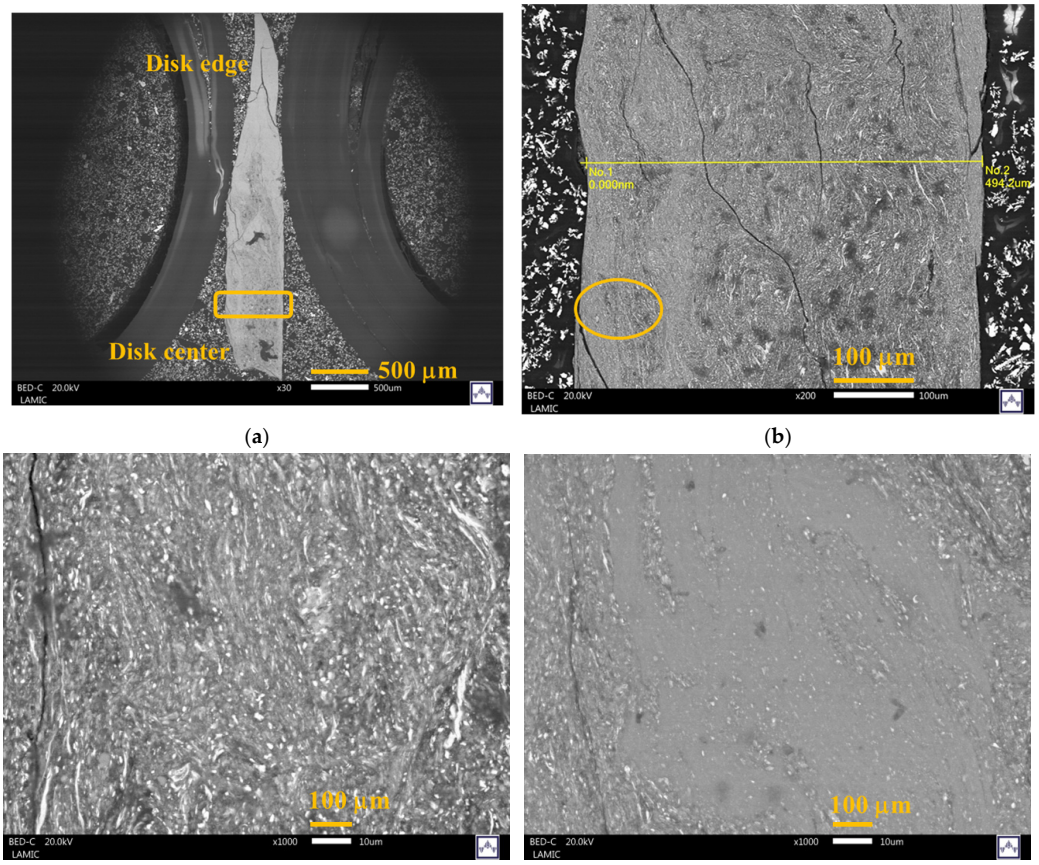

Figure 7. Series of SEM images of HPT-$Mg_2(Co_{1/3}Fe_{1/3}Ni_{1/3})$: (**a**) Transversal section of a disk of HPT-$Mg_2(Co_{1/3}Fe_{1/3}Ni_{1/3})$; (**b**–**d**) progressive zooming of the transversal section of a disk of HPT-$Mg_2(Co_{1/3}Fe_{1/3}Ni_{1/3})$. The yellow rectangle and circle indicate the consecutive zoomed zones.

The corresponding elemental maps of Figure 7c,d are presented in Figure 8a,b, respectively. These figures (and Figures S7 and S8 of the Supplementary File) indicate slightly different compositions in the heterogeneous (Mg 0.443 wt.%, Fe 0.164 wt.%, Co 0.197 wt.%, and Ni 0.196 wt.%) versus the homogeneous (Mg 0.492 wt.%, Fe 0.165 wt.%, Co 0.175 wt.%, and Ni 0.168 wt.%) zones. The nominal composition is: Mg 0.46wt.%, Fe 0.17 wt.%, Co 0.18 wt.%, and Ni 0.18 wt.%. The differences in composition indicate the compositional gradients generated by the HPT process.

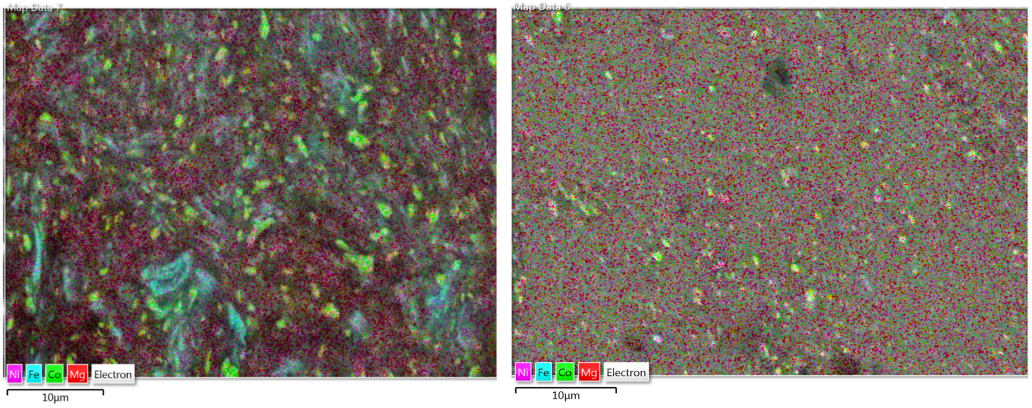

Figure 8. Elemental mappings of HPT-$Mg_2(Co_{1/3}Fe_{1/3}Ni_{1/3})$ in (**a**) a heterogeneous zone and (**b**) a homogeneous zone to demonstrate compositional gradients.

Figure 9 presents the SEM images of the BM-A-$Mg_2(Co_{1/3}Fe_{1/3}Ni_{1/3})$ and HPT-$Mg_2(Co_{1/3}Fe_{1/3}Ni_{1/3})$ after cycling in the hydride state and at low magnification. For the HPT-$Mg_2(Co_{1/3}Fe_{1/3}Ni_{1/3})$, it must be mentioned that this material experienced a complete disintegration of the initial solid into powders. As a result, both materials do not show significant differences in the general morphology of their particles after cycling. The cycled materials also showed flakes corresponding to the less-integrated element: Fe. The cycled material also contains irregular particles larger than 1 µm. The elemental homogeneity of these particles may be associated with the formation of mixed hydrides.

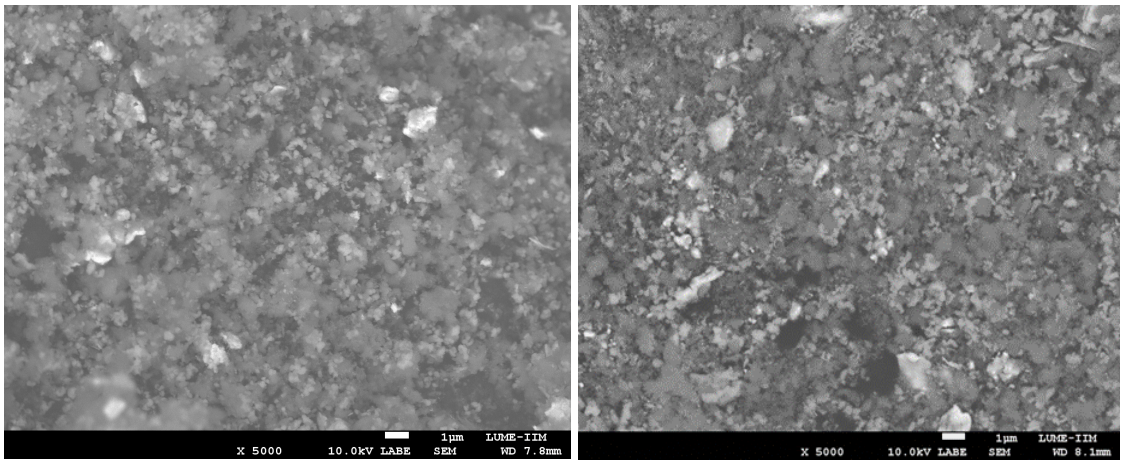

(**a**) (**b**)

Figure 9. SEM images of cycled materials in the hydrided state of (**a**) BM-A-$Mg_2(Co_{1/3}Fe_{1/3}Ni_{1/3})$ and (**b**) HPT-$Mg_2(Co_{1/3}Fe_{1/3}Ni_{1/3})$. 50 complete hydriding/dehydriding cycles and an additional (51st) hydriding.

Figure 10 presents the TEM images of the hydrided BM-A-$Mg_2(Co_{1/3}Fe_{1/3}Ni_{1/3})$ after cycling. The high magnifications of the TEM demonstrated the formation of particles with sizes below 100 nm (Figure S9 in the Supplementary File). The elemental mapping included in Figure 10 indicates a good dispersion of Ni in the Mg matrix, a reasonable dispersion of Co, and a poor integration of Fe. The dispersion of the metals in the material confirms the formation of mixed or partially substituted hydrides of Mg-intermetallics of Ni, Co, and Fe.

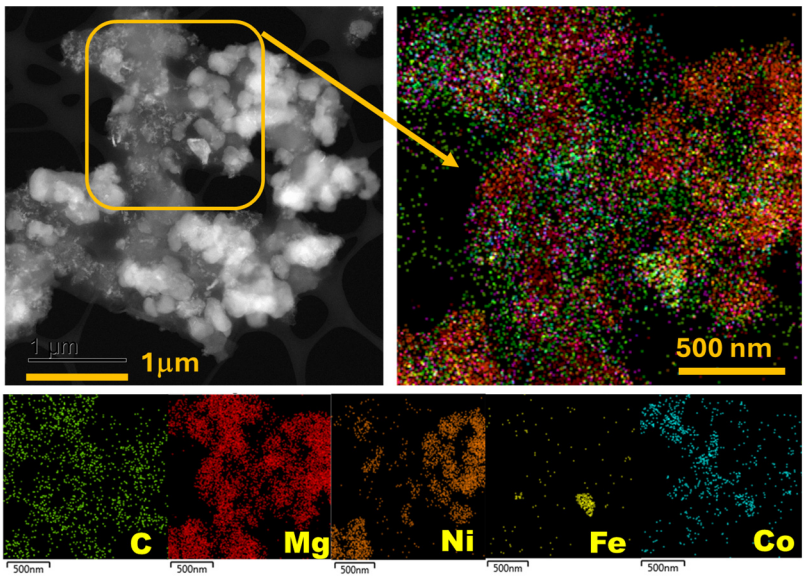

Figure 10. TEM image and elemental mappings of hydrided BM-A-$Mg_2(Co_{1/3}Fe_{1/3}Ni_{1/3})$ after cycling. 50 complete hydriding/dehydriding cycles and an additional (51st) hydriding.

Figure 11 and Figure S10 of the Supplementary File present a series of TEM images of the hydrided HPT-$Mg_2(Co_{1/3}Fe_{1/3}Ni_{1/3})$ after cycling. The TEM images revealed several zones of materials with different structures and chemical compositions at the nanometer scale. The first characteristic is the presence of clear zones of amorphous and crystalline materials (Figures 11 and S10). These zones exhibit notable Mg content. Also, nanocrystals below 100 nm are observed (Figures 11 and S11). In some of these nanocrystals, a relatively high concentration of Fe can be corroborated. The TEM images confirm a better distribution of Ni and Co after cycling, even at the nanometer scale. Figure 11 also suggests a better dispersion of Fe in the HPT-processed material as compared to the BM-A material.

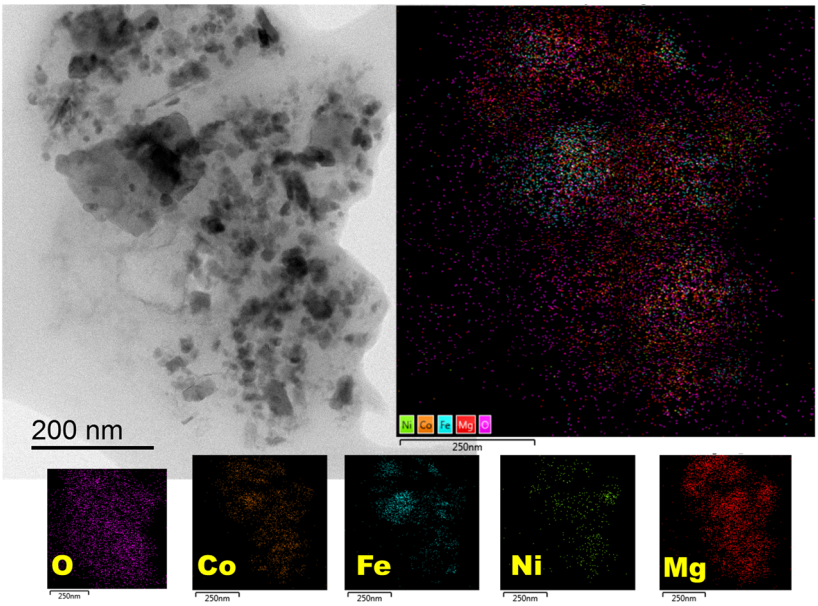

Figure 11. TEM image and elemental mappings of hydrided HPT-$Mg_2(Co_{1/3}Fe_{1/3}Ni_{1/3})$ after cycling. 50 complete hydriding/dehydriding cycles and an additional (51st) hydriding.

The complex ions $[NiH_4]^{-4}$, $[CoH_5]^{-4}$, $[FeH_6]^{-4}$ have distorted tetrahedral, square pyramidal, and octahedral symmetry, respectively [15]. Due to symmetry, the hydrided intermetallics that contain these complex ions can exhibit infrared, Raman, and inelastic neutron scattering signals [15,61,62]. Thus, infrared characterization was used to characterize the hydrided materials BM-A and HPT-$Mg_2(Co_{1/3}Fe_{1/3}Ni_{1/3})$ beyond the limitations of XRD. Table 1 summarizes the reported infrared experimental bands and their assignments for the isoelectronic compounds Mg_2NiH_4, Mg_2CoH_5, and Mg_2FeH_6. However, synthesis conditions (temperature, pressure, reactive ball-milling, etc.) can affect the purity of a hydride. In our experience, incomplete hydriding is the rule rather than the exception. This, in turn, can affect the observed (reported) infrared response. For this reason, it is advisable to include theoretical calculations to compare our experimental results. Figure 12a shows the calculated infrared spectra of Mg_2NiH_4, Mg_2CoH_5, and Mg_2FeH_6. The calculated spectrum of Mg_2NiH_4 indicates that only the compound with Ni presents low-frequency modes (10–200 cm^{-1}). These modes are related to collective Mg-Ni-H motions and lattice vibrations. The most intense peaks occur between 121 and 193 cm^{-1}, whose symmetry is B_u in all cases. Around 200–400 cm^{-1}, all compounds exhibit vibrations dominated by collective lattice movements (Mg-TM and TM-H). The monoclinic Mg_2NiH_4 shows the highest density of peaks, with three transitions near 251 cm^{-1}, 280 cm^{-1}, and 322 cm^{-1}. The fragmentation of these modes reflects the almost complete loss of degeneracy due to the C_2h point group. In contrast, the Mg_2FeH_6 system presents only two well-defined T_{1u} bands in this region (264 cm^{-1} and 280 cm^{-1}). This is a direct consequence of the cubic

symmetry that collects three equivalent vibrational directions into a single degenerate representation. Meanwhile, the tetragonal Mg_2CoH_5 system offers an intermediate scenario: the most intense peak appears at 225 cm^{-1} and corresponds to a pure A_{2u} mode. The line density in this region follows the hierarchy, $C_{2h} > D_{4h} > O_h$, consistent with the loss of degeneracy as symmetry decreases.

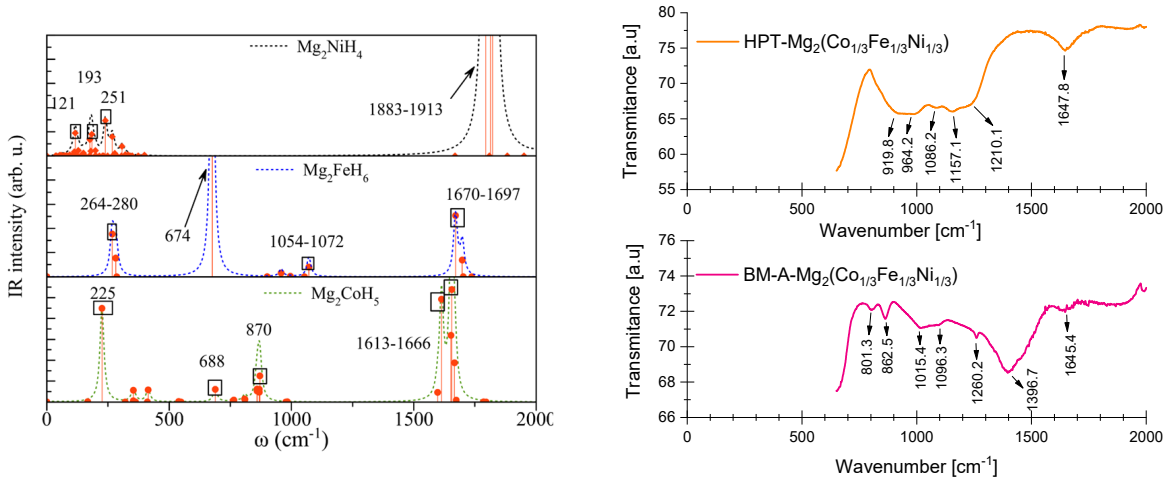

(**a**) (**b**)

Figure 12. (**a**) DFT calculated infrared spectra of Mg_2NiH_4, Mg_2CoH_5, and Mg_2FeH_6 as reference materials. The signals, black squares with red dots, indicate relevant IR characteristics. (**b**) Experimental infrared spectra of hydrided BM-A-$Mg_2(Co_{1/3}Fe_{1/3}Ni_{1/3})$ and HPT-$Mg_2(Co_{1/3}Fe_{1/3}Ni_{1/3})$ after fifty and a half cycles.

In the intermediate region, or the region of activation of internal modes between 400 and 800 cm^{-1}, the three compounds show markedly different behaviors. Firstly, Mg_2NiH_4 does not present modes in that region. In contrast, Mg_2FeH_6 concentrates almost all its intense IR activity in a single mode: a T_{1u} transition at 674 cm^{-1}, which constitutes the most intense signal of all studied materials. This behavior confirms the rigidity of the $[FeH_6]^{-4}$ octahedron and the highly symmetric nature of the local environment. Finally, Mg_2CoH_5 exhibits a group of E_u vibrations in 808–870 cm^{-1}, with moderate intensities, and an additional A_{2u} mode at 684 cm^{-1}. The coexistence of both types of representations reveals an anisotropic coupling characteristic of the tetragonal geometry. In the high-frequency region, the direct metal-hydrogen stretching bands appear well separated and allow evaluation of bond strengths, identified as ν Fe-H ≈ 1670 cm^{-1}, ν Co-H ≈ 1613–1666 cm^{-1}, and ν Ni-H ≈ 1883–1913 cm^{-1}, whose frequency hierarchy is Fe-H > Co-H > Ni-H.

The infrared response of hydrided BM-A-$Mg_2(Co_{1/3}Fe_{1/3}Ni_{1/3})$ and HPT-$Mg_2(Co_{1/3}Fe_{1/3}Ni_{1/3})$ after cycling is presented in Figure 12b. As the main XRD features of the hydrided materials correspond to monoclinic Mg_2NiH_4, the IR spectra are expected to be comparable to that material [61]. However, both hydrided materials exhibit notable differences relative to each other, the calculated reference materials, and the reported reference materials. The hydrided BM-A-$Mg_2(Co_{1/3}Fe_{1/3}Ni_{1/3})$ material presents a prominent peak at 1396.7 cm^{-1} that does not match the calculated or reported bands for any of the three reference materials. The hydrided BM-A-$Mg_2(Co_{1/3}Fe_{1/3}Ni_{1/3})$ also presents a series of small peaks located at about 800–862 cm^{-1}, 1015–1096 cm^{-1}, and 1260.2 cm^{-1}. A small peak partially matches the expected peaks at about 1650 cm^{-1} for Mg_2FeH_6 and Mg_2CoH_5. For its part, in the HPT-$Mg_2(Co_{1/3}Fe_{1/3}Ni_{1/3})$ hydrided material, the experimental peak at 1086.2 cm^{-1} is more consistent with the δ Co-H (E) for Mg_2CoH_5 observed by Parker et al. [62] and the calculated peaks at 1054–1072 cm^{-1} for the Mg_2FeH_6. Meanwhile,

the peak at 1674.8 cm^{-1} coincides with calculated peaks for Mg_2CoH_5 and Mg_2FeH_6, as well as the experimentally observed peak in Mg_2NiH_4 [61]. The strong infrared band at 1674 cm^{-1} can be attributed to ν_1 and ν_3 vibrational modes [61]. The peaks in the region 900–1200 cm^{-1} can be related to δ TM-H. Overall, the infrared peaks indicate the formation of mixed hydrided intermetallics, resulting from the partial substitution of Co, Fe, and Ni in the corresponding hydrided intermetallics with Mg [15]. In other words, the hydrided BM-A-$Mg_2(Co_{1/3}Fe_{1/3}Ni_{1/3})$ and HPT-$Mg_2(Co_{1/3}Fe_{1/3}Ni_{1/3})$ are more than a simple mixture of Mg_2NiH_4, Mg_2CoH_5, and Mg_2FeH_6. Infrared spectroscopy characterization and the comparison to reference materials, calculated and reported, indicated that the hydrided BM-A-$Mg_2(Co_{1/3}Fe_{1/3}Ni_{1/3})$ and HPT-$Mg_2(Co_{1/3}Fe_{1/3}Ni_{1/3})$ are multi-element Mg-based complex materials [2,63].

Table 1. Reported band assignments of the infrared spectra of the hydrided intermetallic magnesium complex.

Material	Peak/Band [cm^{-1}]	Assignation	Reference
Mg_2NiH_4	1674 s	ν Ni-H (T_2)	[61]
	791 m	δ Ni-H (E)	
	745 m	δ Ni-H (E)	
	618 s	δ Ni-H (T_2)	
	528 sh	Libration (T_1)	
Mg_2CoH_5	1757 s	ν Co-H (E)	[62]
	1632 s	ν Co-H (A_1)	
	1032 br, w	δ Co-H (E)	
	869 s	δ Co-H (E)	
	766 w	δ Co-H (A_1)	
	574 w	Libration (E)	
	522 w	Libration (E)	
Mg_2FeH_6	1912 w	δ Fe-H (T_{2g})	[64]
	1843	δ Fe-H (T_{2g}) + δ Fe-H (T_{2u})	
	1746 vs	ν Fe-H (T^{1u})	

ν: stretch, δ: bend, s: strong, m: medium, w: weak, br: broad, sh: shoulder, vs: very strong.

4. Discussion

4.1. Reasons for the Observed Hydrogen Storage Performance

The hydrogen storage performance of the materials is discussed based on three fundamental characteristics:

1. Hydrogen uptake and release. In general, both BM-A-$Mg_2(Co_{1/3}Fe_{1/3}Ni_{1/3})$ and HPT-$Mg_2(Co_{1/3}Fe_{1/3}Ni_{1/3})$ materials present good hydriding/dehydriding kinetics. The partial substitution of Co, Fe, or both has been reported in Mg or Mg-Ni alloys [15,65–67]. The presence of the different metals Co, Fe, and Ni in the studied materials maintains a synergistic effect as previously observed [17,18,68], and it may be responsible for the good kinetics. The $Mg_2(Co_{1/3}Fe_{1/3}Ni_{1/3})$ materials exhibit lower-than-expected (vs. theoretical), but still acceptable, hydrogen storage values during cycling. In this characteristic, the BM-A-$Mg_2(Co_{1/3}Fe_{1/3}Ni_{1/3})$ material presented better performance, including superior PCT behavior. The lower-than-expected hydrogen uptake can be attributed to limited Fe integration, insufficient activation or reactivation, the relatively low hydriding pressure (15 bar), and the reaction time used in our experiments.

Overall, the onset temperatures and the hydrogen uptake are better than those reported in other studies. For example, dehydriding temperatures of the $Mg_2(Co_{1/3}Fe_{1/3}Ni_{1/3})$ materials are lower than dehydriding temperatures of pure Mg_2NiH_4 [69,70]. A PCT test of

a multi-element Mg-based complex hydride of the same composition as the one presented in this project, but produced by hydrogen-reactive ball-milling, indicated a hydrogen uptake of 2.8 wt.% at pressures up to 20 bar and 300 °C [71]. Thus, annealing and the HPT process are effective in improving the hydrogen storage capacity, with annealing being more effective than the HPT. However, concentration gradients, inhomogeneities, and incomplete integration of Fe could diminish the effectiveness of HPT. It is possible that other experimental conditions in the HPT process will improve Fe mixing. Also, further optimization of the concentrations and distribution of Co, Fe, and Ni is required.

Activation can be achieved by heating in a vacuum for a period of time or by performing a certain number of hydriding/dehydriding cycles. Activation by cycling is a well-established approach to improving hydrogen storage capacity and kinetics. Deactivation caused by the sorption of impurities present in hydrogen gas or protective atmospheres is a well-known degradation mechanism in the hydrogen storage materials. Reactive impurities can be permanently sorbed in hydrogen storage materials. However, handling in the open air during HPT processing of $Mg_2(Co_{1/3}Fe_{1/3}Ni_{1/3})$ did not significantly reduce hydrogen uptake compared to the BM-A material. This comparison is made on fully activated materials; in this state, a difference of only 0.3 wt.% is registered. The ball-milled materials were always handled under a protective atmosphere of high-purity argon, whereas the HPT process was performed in open air. Jiang et al., in a theoretical study of O_2 surface poisoning in multicomponent alloys, indicated that O_2 adsorbs on Fe sites [72]. In the $Mg_2(Co_{1/3}Fe_{1/3}Ni_{1/3})$, the Fe and Mg are particularly suitable sites for oxidation. Surface oxides are not always detected by XRD because they can be nanometer-sized or amorphous. Other techniques besides XRD must be used to detect surface oxides. However, in our experience with hydrogen storage materials, the presence of oxide layers is unavoidable even under protective atmospheres. Surface oxides certainly reduce hydrogen uptake. This effect is not clearly evident in the HPT-$Mg_2(Co_{1/3}Fe_{1/3}Ni_{1/3})$ material. However, the hydrogen release is incomplete in the HPT material, requiring a dynamic vacuum to complete the reaction.

On the other hand, heating under dynamic vacuum for several hours can remove some impurities initially present in H_2 gas or protective atmospheres. Chemically inert gases such as N_2 and CO_2 can form a blocking layer on the alloy surface, thereby physically hindering H_2 from reaching active sites [73,74]. Unexpectedly, in the after-cycled materials, heating under dynamic vacuum before PCT testing, combined with the extended reaction time in PCT, produced better hydrogen uptake than in the as-prepared materials. This can be understood as a reactivation process of the materials. However, the PCT curves after cycling showed increased hysteresis, which can be related to another degradation process discussed in the next subsection.

Regarding the hydriding pressure, other reports on the formation of Mg_2NiH_4, Mg_2CoH_5, or Mg_2FeH_6 used pressures as high as 20–70 bar, and even in many cases, the hydriding reaction is not complete [14,69,75–78]. This means that increasing hydrogen pressure or temperature can increase hydrogen uptake. However, considering that using low hydrogen gas pressure is economically, technologically, and safely feasible, we use 15 bar as the initial hydriding pressure.

2. Onset temperatures. The onset temperatures of hydriding and dehydriding reactions can be influenced by factors such as material activation and structure. The full activation of materials was particularly difficult in the HPT-processed material. This behavior is due to the significant decrease in the active surface caused by the formation of a consolidated block of material under the high compression pressure used in the HPT process. Once fully activated, the HPT-processed material exhibited a small improvement in onset temperatures compared with the BM-A material. This is

particularly evident in the dehydriding reactions. Assila et al. proposed that strains applied to Mg_2NiH_4 can reduce its stability [79]. These results were obtained in a DFT study [79], but their findings can explain the reduction in the onset temperature observed in our HPT-processed material.

3. Cyclability and expected durability. In both criteria, the BM-A-$Mg_2(Co_{1/3}Fe_{1/3}Ni_{1/3})$ performs better, based on the complete hydrogen release and the expected durability inferred from fitting the maximum hydrogen uptake versus cycle number. Meanwhile, the HPT-$Mg_2(Co_{1/3}Fe_{1/3}Ni_{1/3})$ exhibited reasonable reversibility and cyclability under the test conditions. The present results on cycling stability are difficult to compare with other Mg-intermetallic materials because no similar sample production and composition have been reported. However, a few examples are listed below. Binary materials, such as Mg-Ni, Mg-Co, or Mg-Fe, can serve as a starting point for comparison: Mg-25Ni is reported to exhibit excellent cyclic stability with minimal capacity loss over 10 cycles at 20/0.1 bar and a series of temperatures, including 300 °C [80]. However, the number of cycles is too limited to detect performance loss. Fadonougbo et al. demonstrated cycling stability in a 1000-cycle test for Mg-Ni composites (16.3, 11.3, or 4.4 at.% Ni) [81]. They indicated that the reason is the high microstructural stability of the Mg-Ni mixtures produced by induction melting [81]. However, as observed in a plot of the hydrogen storage capacity versus the number of cycles in that report [81], full activation was achieved at the 100th cycle. Puszkiel et al. performed an analysis of 1000 hydriding/dehydriding cycles of Mg-Fe [82]. A continuous reduction in hydrogen storage was observed in that work, with a maximum capacity of about 2.9 wt.% [82]. HPT-processed ZK60 alloy (Mg-5Zn-0.8Zr) was reported to be stable after 200 hydriding/dehydriding cycles [36] with a hydrogen uptake slightly superior to 3.5 wt.%. As shown above, the number of cycles and the cycling conditions themselves are difficult to compare. Moreover, the percentage of decrease in hydrogen storage capacity is not always reported. The data presented above indicate that the BM-A and HPT-processed $Mg_2(Co_{1/3}Fe_{1/3}Ni_{1/3})$ materials exhibit reasonable cyclability and are suitable for further testing in larger tanks. On the other hand, as described in the characterization section, the material underwent several structural changes across the different stages of production and testing.

4.2. Structure Evolution of the Materials and Their Effect on Hydrogen Storage Performance

Knowing that simple ball-milling of $Mg_2(Co_{1/3}Fe_{1/3}Ni_{1/3})$ demonstrated limitations in achieving dispersion of Ni, Co, and Fe in the Mg matrix [18]; annealing and HPT were performed to improve metal dispersion in the Mg matrix and to promote intermetallic formation in the hydrided state. Temperature and duration of the different processes can play an important role in the structure evolution: it is estimated that the local temperature during ball–ball collisions can reach up to 600 °C, depending on several milling conditions [83]. Annealing was performed at 350 °C. Regarding HTP processing, there is no consensus on the increase in temperature caused by friction between the rotating and fixed anvils, but in general, it is small (10–45 °C) [84]. The cycling was performed by heating between 300 and 350 °C. The HTP processing time is considered short, about 10–15 min per disk. Meanwhile, the annealing was 6 h. Cycling lasted about 35–40 working days to complete the 50-cycle testing. Among the structural characteristics of the HPT material is that the Mg_2Ni peaks of Figure 3 (after 10 turns in HPT) are relatively more intense than those in a 2Mg-Ni mixture processed by 100 turns in HPT [42]. It has been reported that there is some difficulty in the complete formation of Mg_2Ni from the elements by heating in a vacuum, arc melting, or severe plastic deformation processes [42,85–87]. Improvements in the formation of intermetallics such as Mg_2Ni can be achieved by careful selection of

the experimental conditions and preparation techniques, for example, by varying metal stoichiometries or combining high-energy ball milling with HPT [88,89]. The formation of Mg_2Ni in our samples was due to the combination of ball milling and annealing that preceded the HPT process. The XRD indicates the formation of texture in the Mg and Mg_2Ni phases after HPT. The texture observed after HPT was also reported in other works [38]. However, because the texture is missing after cycling, this cannot account for the differences observed in hydrogen storage capacity.

On the other hand, many structural changes occur during/upon cycling: the HPT-processed material experienced severe decrepitation, transforming from a solid to a fine powder. Decrepitation can improve hydrogen storage performance in the first cycles by exposing fresh surfaces. In the long term, issues such as reduced thermal conductivity between small particles produced by decrepitation can affect hydrogen storage. However, the SEM images showed virtually no difference between the decrepitated HPT materials and the BM-A materials after cycling. Thus, despite being a degradation effect, the decrepitation is not the main reason for the decrease in hydrogen storage capacity after cycling. Other structural changes upon cycling include the formation of hydride phases, small shifts from the expected peak positions, changes in relative peak intensities (texture), and the appearance of an unidentified peak observed in XRD after cycling. SEM and TEM also reveal changes, including improved dispersion of Ni, Co, and, to a lesser extent, Fe in the Mg matrix. Thus, the main changes were due to cycling.

Diffusion of atoms in grain boundaries [90] can occur during different processes. The successive heating and cooling in a hydrogen atmosphere/vacuum, and the nucleation and growth mechanisms of the hydride phases, can improve the dispersion of the components in the Mg matrix as observed in TEM images. A more disordered material can be related to the changes observed in the after-cycling hydriding and dehydriding equilibrium pressure of PCT curves, where a larger hysteresis is evident. The hysteresis in PCT curves can be related to crystal lattice mismatches, in our case, augmented by the presence of different metals, Co, Fe, and Ni. This leads to more lattice and boundary defects. This suggests a tendency toward the formation of highly disordered intermetallics [63,91–93].

5. Conclusions

Two $Mg_2(Co_{1/3}Fe_{1/3}Ni_{1/3})$ materials, produced through a complex process comprising ball milling, annealing, and high-pressure torsion, were tested in 50 hydriding/dehydriding cycles. Considering several factors related to hydrogen storage capacity, hydrogen release, onset temperatures, durability, and degradation mechanisms, the $Mg_2(Co_{1/3}Fe_{1/3}Ni_{1/3})$ material processed by ball-milling and annealing (BM-A) exhibits better performance than the material processed by HPT.

XRD, SEM and TEM characterization indicate the structural evolution of the $Mg_2(Co_{1/3}Fe_{1/3}Ni_{1/3})$ materials. Infrared spectroscopy confirms the formation of hydrided intermetallics with partial substitution of Co, Ni, and Fe. Processing and cycling improve Ni and Co dispersion in the Mg matrix and promote nanocrystal formation as a result of applied temperatures (300–350 °C) and times (35–40 days). However, unreacted Fe remains. This implies incomplete hydriding reactions and the need to optimize Fe content. Still, the $Mg_2(Co_{1/3}Fe_{1/3}Ni_{1/3})$ materials present adequate performance to continue further research on this material. Further research is needed to increase the test mass from a small sample holder (300 mg) to a tank of a relevant size (tens or hundreds of grams).

Supplementary Materials: The following supporting information can be downloaded at https://www.mdpi.com/article/10.3390/met16040435/s1, Figure S1. Temperature programmed hydriding and dehydriding cycles of BM-A-$Mg_2(Co_{1/3}Fe_{1/3}Ni_{1/3})$. (a) Hydriding cycles 1–10. (b) Dehydriding cycles 1–10. (c) Hydriding cycles 11–20. (d) Dehydriding cycles 11–20. Figure S2. Temperature-

programmed hydriding and dehydriding cycles of BM-A-$Mg_2(Co_{1/3}Fe_{1/3}Ni_{1/3})$. (a) Hydriding cycles 21–30. (b) Dehydriding cycles 21–30. (c) Hydriding cycles 31–40. (d) Dehydriding cycles 31–40. (e) Hydriding cycles 41–50. (f) Dehydriding cycles 41–50. Figure S3. Temperature-programmed hydriding and dehydriding cycles of HPT-$Mg_2(Co_{1/3}Fe_{1/3}Ni_{1/3})$. (a) Hydriding cycles 1–10. (b) Dehydriding cycles 1–10. (c) Hydriding cycles 11–20. (d) Dehydriding cycles 11–20. Figure S4. Temperature-programmed hydriding and dehydriding cycles of HPT-$Mg_2(Co_{1/3}Fe_{1/3}Ni_{1/3})$. (a) Hydriding cycles 21–30. (b) Dehydriding cycles 21–30. (c) Hydriding cycles 31–40. (d) Dehydriding cycles 31–40. (e) Hydriding cycles 41–50. (f) Dehydriding cycles 41–50. Figure S5. Traces of the tenth, twenty-fifth, and fiftieth (a) hydriding at 15 bar and (b) dehydriding at 0.015 bar reactions of the BM-A-$Mg_2(Co_{1/3}Fe_{1/3}Ni_{1/3})$ and HPT-$Mg_2(Co_{1/3}Fe_{1/3}Ni_{1/3})$. Figure S6. (a) PCT curves of as-prepared BM-A-$Mg_2(Co_{1/3}Fe_{1/3}Ni_{1/3})$ and HPT-$Mg_2(Co_{1/3}Fe_{1/3}Ni_{1/3})$, and after cycling BM-A-$Mg_2(Co_{1/3}Fe_{1/3}Ni_{1/3})$ and HPT-$Mg_2(Co_{1/3}Fe_{1/3}Ni_{1/3})$. The black dotted line indicates the equilibrium for the reference system Mg/MgH_2. (b) PCT curves of the fragmented disks of HPT-$Mg_2(Co_{1/3}Fe_{1/3}Ni_{1/3})$. HH hydriding. dhh dehydriding. Figure S7. Elemental quantification of HPT-$Mg_2(Co_{1/3}Fe_{1/3}Ni_{1/3})$, heterogeneous zone. Figure S8. Elemental quantification of HPT-$Mg_2(Co_{1/3}Fe_{1/3}Ni_{1/3})$, homogeneous zone. Figure S9. A series of TEM images after cycling test (hydride form) of BM-A-$Mg_2(Co_{1/3}Fe_{1/3}Ni_{1/3})$. Figure S10. A series of TEM images of HPT-$Mg_2(Co_{1/3}Fe_{1/3}Ni_{1/3})$ in the hydrided state after cycling. Figure S11. Elemental mapping of HPT-processed $Mg_2(Co_{1/3}Fe_{1/3}Ni_{1/3})$ in the hydrided state after cycling.

Author Contributions: Conceptualization, K.S.-A.; methodology, K.S.-A., J.E.G.-H., J.M.C.-S., E.M.-A. and R.L.-J.; validation, N.L.T.-G.; formal analysis, K.S.-A. and E.M.-A.; investigation, N.L.T.-G., P.d.C.C.-N., J.E.G.-H., J.M.C.-S., E.M.-A. and R.L.-J.; resources, K.S.-A., J.E.G.-H., J.M.C.-S., E.M.-A. and R.L.-J.; data curation, N.L.T.-G.; writing—original draft preparation, K.S.-A. and E.M.-A.; writing—review and editing, P.d.C.C.-N. and K.S.-A.; visualization, N.L.T.-G.; supervision, K.S.-A.; project administration, K.S.-A.; funding acquisition, K.S.-A. All authors have read and agreed to the published version of the manuscript.

Funding: This research was funded by CONAHCYT (SECIHTI), CF-2023-I-394: Aleaciones de alta entropía con V o Mg para el almacenamiento de hidrógeno. N. L. Torres Garcia acknowledges SECIHTI for the postdoctoral fellowship under the academic modality of the program "Estancias Posdoctorales por México 2022 (3)–Renovación". P.C. Cintron Nuñez gratefully acknowledges the support of a graduate fellowship from CONAHCYT (SECIHTI), México. E. Martínez-Aguilar thanks SECIHTI for the postdoctoral fellowship No. MOD.ORD.11/2025 2022, and 2023. R. López-Juárez thanks DGAPA-UNAM for financial support under project number PAPIIT-IN105325.

Data Availability Statement: The data presented in this study are available on request from the corresponding author. The data are not publicly available due to the volume of cycling test data.

Acknowledgments: The authors acknowledge Orlando Hernández Cristobal for the SEM studies. The authors thank Omar Novelo Peralta and Josué Esau Romero Ibarra from LUME RRID: SCR_024400, for SEM and TEM image acquisition and technical support.

Conflicts of Interest: The authors declare no conflicts of interest.

References

1. Allendorf, M.D.; Stavila, V.; Snider, J.L.; Witman, M.; Bowden, M.E.; Brooks, K.; Tran, B.L.; Autrey, T. Challenges to Developing Materials for the Transport and Storage of Hydrogen. *Nat. Chem.* **2022**, *14*, 1214–1223. [CrossRef]
2. Lin, H.-J.; Lu, Y.-S.; Zhang, L.-T.; Liu, H.-Z.; Edalati, K.; Révész, Á. Recent Advances in Metastable Alloys for Hydrogen Storage: A Review. *Rare Met.* **2022**, *41*, 1797–1817. [CrossRef]
3. Xu, Y.; Zhou, Y.; Li, Y.; Hao, Y.; Wu, P.; Ding, Z. Recent Advances in the Preparation Methods of Magnesium-Based Hydrogen Storage Materials. *Molecules* **2024**, *29*, 2451. [CrossRef]
4. de Rango, P.; Wen, J.; Skryabina, N.; Laversenne, L.; Fruchart, D.; Borges, M. Hydrogen Storage Properties of Mg-Ni Alloys Processed by Fast Forging. *Energies* **2020**, *13*, 3509. [CrossRef]
5. Møller, K.T.; Jensen, T.R.; Akiba, E.; Li, H. Hydrogen—A Sustainable Energy Carrier. *Prog. Nat. Sci. Mater. Int.* **2017**, *27*, 34–40. [CrossRef]

6. Chen, Z.; Ma, Z.; Zheng, J.; Li, X.; Akiba, E.; Li, H.-W. Perspectives and Challenges of Hydrogen Storage in Solid-State Hydrides. *Chin. J. Chem. Eng.* **2021**, *29*, 1–12. [CrossRef]
7. Yang, M.; Hunger, R.; Berrettoni, S.; Sprecher, B.; Wang, B. A Review of Hydrogen Storage and Transport Technologies. *Clean Energy* **2023**, *7*, 190–216. [CrossRef]
8. Li, Q.; Lu, Y.; Luo, Q.; Yang, X.; Yang, Y.; Tan, J.; Dong, Z.; Dang, J.; Li, J.; Chen, Y.; et al. Thermodynamics and Kinetics of Hydriding and Dehydriding Reactions in Mg-Based Hydrogen Storage Materials. *J. Magnes. Alloys* **2021**, *9*, 1922–1941. [CrossRef]
9. Mezbahul-Islam, M.; Mostafa, A.O.; Medraj, M. Essential Magnesium Alloys Binary Phase Diagrams and Their Thermochemical Data. *J. Mater.* **2014**, *2014*, 704283. [CrossRef]
10. Paul, A.R.; Mehla, S.; Bhargava, S. Intermetallic Compounds for Hydrogen Storage: Current Status and Future Perspectives. *Small* **2024**, *21*, 2408889. [CrossRef]
11. Pavlyuk, N.; Kordan, V.; Dmytriv, G.; Yarema, M.; Pavlyuk, V. Intermetallic Materials for High-Capacity Hydrogen Storage Systems. *Chimia* **2024**, *78*, 869–877. [CrossRef]
12. Liu, Y.; Chabane, D.; Elkedim, O. Intermetallic Compounds Synthesized by Mechanical Alloying for Solid-State Hydrogen Storage: A Review. *Energies* **2021**, *14*, 5758. [CrossRef]
13. Ren, L.; Li, Y.; Zhang, N.; Li, Z.; Lin, X.; Zhu, W.; Lu, C.; Ding, W.; Zou, J. Nanostructuring of Mg-Based Hydrogen Storage Materials: Recent Advances for Promoting Key Applications. *Nano-Micro Lett.* **2023**, *15*, 93. [CrossRef]
14. Zepon, G.; Leiva, D.R.; Kaufman, M.J.; Figueroa, S.J.A.; Floriano, R.; Lamas, D.G.; Asselli, A.A.C.; Botta, W.J. Controlled Mechanochemical Synthesis and Hydrogen Desorption Mechanisms of Nanostructured Mg_2CoH_5. *Int. J. Hydrogen Energy* **2015**, *40*, 1504–1515. [CrossRef]
15. Barale, J.; Deledda, S.; Dematteis, E.M.; Sørby, M.H.; Baricco, M.; Hauback, B.C. Synthesis and Characterization of Magnesium-Iron-Cobalt Complex Hydrides. *Sci. Rep.* **2020**, *10*, 9000. [CrossRef] [PubMed]
16. Liu, Y.; Yue, M.; Guo, Y.; Jiang, Y.; Sun, Y.; Feng, L.; Wang, Y. Catalytic Effect of Carbon-Supported NiCoFeCuMg High-Entropy Alloy Nanocatalysts on Hydrogen Storage Properties of MgH_2. *J. Magnes. Alloys* **2025**, *13*, 1232–1242. [CrossRef]
17. Jiang, Y.-B.; Jiang, W.; Si, N.; Wang, Z. Hydrogen Storage Properties of MgH_2 + Mg_2NiH_4–Co/C Ternary Nanocomposite. *Int. J. Hydrogen Energy* **2024**, *72*, 258–267. [CrossRef]
18. Ruiz-Santacruz, E.D.; Núñez, P.d.C.C.; García, N.L.T.; Suárez-Alcántara, K. $Mg_2(Co_{1/3}Fe_{1/3}Ni_{1/3})$, $Mg_2(Cu_{1/3}Fe_{1/3}Ni_{1/3})$, $Mg_2(Co_{1/3}Cu_{1/3}Fe_{1/3})$, $Mg_2(Co_{1/3}Cu_{1/3}Ni_{1/3})$, and $Mg_2(Co_{1/4}Cu_{1/4}Fe_{1/4}Ni_{1/4})$ Materials for Hydrogen Storage. *Inorganics* **2025**, *13*, 135. [CrossRef]
19. De Lima, G.F.; Leiva, D.R.; Ishikawa, T.T.; Bolfarini, C.; Kiminami, C.S.; Botta Filho, W.J.; Jorge, A.M. Hydrogen Sorption Properties of the Complex Hydride Mg_2FeH_6 Consolidated by HPT. In *Materials Science Forum*; Trans Tech Publications Ltd.: Baech, Switzerland, 2010; Volume 667–669, pp. 1053–1058. [CrossRef]
20. Edalati, K.; Bachmaier, A.; Beloshenko, V.A.; Beygelzimer, Y.; Blank, V.D.; Botta, W.J.; Bryła, K.; Čížek, J.; Divinski, S.; Enikeev, N.A.; et al. Nanomaterials by Severe Plastic Deformation: Review of Historical Developments and Recent Advances. *Mater. Res. Lett.* **2022**, *10*, 163–256. [CrossRef]
21. Edalati, K.; Horita, Z. A Review on High-Pressure Torsion (HPT) from 1935 to 1988. *Mater. Sci. Eng. A* **2016**, *652*, 325–352. [CrossRef]
22. Valiev, R.Z.; Straumal, B.; Langdon, T.G. Using Severe Plastic Deformation to Produce Nanostructured Materials with Superior Properties. *Annu. Rev. Mater. Res.* **2022**, *52*, 357–382. [CrossRef]
23. Révész, Á.; Gajdics, M. High-Pressure Torsion of Non-Equilibrium Hydrogen Storage Materials: A Review. *Energies* **2021**, *14*, 819. [CrossRef]
24. Edalati, K.; Akiba, E.; Botta, W.J.; Estrin, Y.; Floriano, R.; Fruchart, D.; Grosdidier, T.; Horita, Z.; Huot, J.; Li, H.-W.; et al. Impact of Severe Plastic Deformation on Kinetics and Thermodynamics of Hydrogen Storage in Magnesium and Its Alloys. *J. Mater. Sci. Technol.* **2023**, *146*, 221–239. [CrossRef]
25. Edalati, K. Severe Plastic Deformation of Light Metals (Magnesium, Aluminum and Titanium) and Alloys by High-Pressure Torsion: Review of Fundamentals and Mechanical/Functional Properties. *Mater. Trans.* **2024**, *65*, 466–480. [CrossRef]
26. Edalati, K. Review of Advances in High-Pressure Torsion of Titanium and Ti-Based Materials (Alloys, Intermetallics, Oxides and High-Entropy Compounds). *Mater. Trans.* **2025**, *66*, 464–478. [CrossRef]
27. Edalati, K.; Yamamoto, A.; Horita, Z.; Ishihara, T. High-Pressure Torsion of Pure Magnesium: Evolution of Mechanical Properties, Microstructures and Hydrogen Storage Capacity with Equivalent Strain. *Scr. Mater.* **2011**, *64*, 880–883. [CrossRef]
28. Révész, Á.; Kánya, Z.; Verebélyi, T.; Szabó, P.J.; Zhilyaev, A.P.; Spassov, T. The Effect of High-Pressure Torsion on the Microstructure and Hydrogen Absorption Kinetics of Ball-Milled $Mg_{70}Ni_{30}$. *J. Alloys Compd.* **2010**, *504*, 83–88. [CrossRef]
29. Grosdidier, T.; Fundenberger, J.J.; Zou, J.X.; Pan, Y.C.; Zeng, X.Q. Nanostructured Mg Based Hydrogen Storage Bulk Materials Prepared by High Pressure Torsion Consolidation of Arc Plasma Evaporated Ultrafine Powders. *Int. J. Hydrogen Energy* **2015**, *40*, 16985–16991. [CrossRef]

30. He, L.; Shi, X.; Li, X.; Huang, J.; Cheng, T.; Wang, X.; Li, Y.; Lin, H.; Edalati, K.; Li, H.-W. Severe Plastic Deformation through High-Pressure Torsion for Preparation of Hydrogen Storage Materials—A Review. *Mater. Trans.* **2023**, *64*, 1575–1584. [CrossRef]
31. Edalati, K.; Matsuda, J.; Arita, M.; Daio, T.; Akiba, E.; Horita, Z. Mechanism of Activation of TiFe Intermetallics for Hydrogen Storage by Severe Plastic Deformation Using High-Pressure Torsion. *Appl. Phys. Lett.* **2013**, *103*, 143902. [CrossRef]
32. Edalati, K.; Matsuo, M.; Emami, H.; Itano, S.; Alhamidi, A.; Staykov, A.; Smith, D.J.; Orimo, S.; Akiba, E.; Horita, Z. Impact of Severe Plastic Deformation on Microstructure and Hydrogen Storage of Titanium-Iron-Manganese Intermetallics. *Scr. Mater.* **2016**, *124*, 108–111. [CrossRef]
33. Leiva, D.R.; Jorge, A.M.; Ishikawa, T.T.; Huot, J.; Fruchart, D.; Miraglia, S.; Kiminami, C.S.; Botta, W.J. Nanoscale Grain Refinement and H-Sorption Properties of MgH_2 Processed by High-Pressure Torsion and Other Mechanical Routes. *Adv. Eng. Mater.* **2010**, *12*, 786–792. [CrossRef]
34. Hongo, T.; Edalati, K.; Arita, M.; Matsuda, J.; Akiba, E.; Horita, Z. Significance of Grain Boundaries and Stacking Faults on Hydrogen Storage Properties of Mg_2Ni Intermetallics Processed by High-Pressure Torsion. *Acta Mater.* **2015**, *92*, 46–54. [CrossRef]
35. Edalati, K.; Uehiro, R.; Ikeda, Y.; Li, H.-W.; Emami, H.; Filinchuk, Y.; Arita, M.; Sauvage, X.; Tanaka, I.; Akiba, E.; et al. Design and Synthesis of a Magnesium Alloy for Room Temperature Hydrogen Storage. *Acta Mater.* **2018**, *149*, 88–96. [CrossRef]
36. Grill, A.; Horky, J.; Panigrahi, A.; Krexner, G.; Zehetbauer, M. Long-Term Hydrogen Storage in Mg and ZK60 after Severe Plastic Deformation. *Int. J. Hydrogen Energy* **2015**, *40*, 17144–17152. [CrossRef]
37. de Marco, M.O.; Li, Y.; Li, H.-W.; Edalati, K.; Floriano, R. Mechanical Synthesis and Hydrogen Storage Characterization of MgVCr and MgVTiCrFe High-Entropy Alloy. *Adv. Eng. Mater.* **2020**, *22*, 1901079. [CrossRef]
38. Yan, Z.; Zhu, J.; Zhang, Z.; Wang, Q.; Xue, Y. The Microstructural, Textural, and Mechanical Effects of High-Pressure Torsion Processing on Mg Alloys: A Review. *Front. Mater.* **2022**, *9*, 964992. [CrossRef]
39. Nazeer, F.; Long, J.; Yang, Z.; Li, C. Superplastic Deformation Behavior of Mg Alloys: A-Review. *J. Magnes. Alloys* **2022**, *10*, 97–109. [CrossRef]
40. Osorio-García, M.; Suárez-Alcántara, K.; Todaka, Y.; Tejeda-Ochoa, A.; Herrera-Ramírez, M.; Hernández-Silva, O.; Cruz-Gandarilla, F.; Cabañas-Moreno, J.G. Low-Temperature Hydrogenation of Mg-Ni-Nb_2O_5 Alloy Processed by High-Pressure Torsion. *J. Alloys Compd.* **2021**, *878*, 160309. [CrossRef]
41. Zhang, J.; Li, Z.; Wu, Y.; Guo, X.; Ye, J.; Yuan, B.; Wang, S.; Jiang, L. Recent Advances on the Thermal Destabilization of Mg-Based Hydrogen Storage Materials. *RSC Adv.* **2019**, *9*, 408–428. [CrossRef] [PubMed]
42. López Gómez, E.I.; Gonzalez, J.; Cubero-Sesin, J.M.; Huot, J. Synthesis of Nanostructured Mg_2Ni for Hydrogen Storage by Mechanical Alloying via High-Pressure Torsion. *Reactions* **2024**, *5*, 651–663. [CrossRef]
43. Carrillo-Bucio, J.L.; Tena-Garcia, J.R.; Armenta-Garcia, E.P.; Hernandez-Silva, O.; Cabañas-Moreno, J.G.; Suárez-Alcántara, K. Low-Cost Sieverts-Type Apparatus for the Study of Hydriding/Dehydriding Reactions. *HardwareX* **2018**, *4*, e00036. [CrossRef]
44. Baran, A.; Polański, M. Magnesium-Based Materials for Hydrogen Storage—A Scope Review. *Materials* **2020**, *13*, 3993. [CrossRef]
45. Xu, Y.; Zhou, Y.; Li, Y.; Hao, Y.; Wu, P.; Ding, Z. Magnesium-Based Hydrogen Storage Alloys: Advances, Strategies, and Future Outlook for Clean Energy Applications. *Molecules* **2024**, *29*, 2525. [CrossRef]
46. Giannozzi, P.; Baroni, S.; Bonini, N.; Calandra, M.; Car, R.; Cavazzoni, C.; Ceresoli, D.; Chiarotti, G.L.; Cococcioni, M.; Dabo, I.; et al. QUANTUM ESPRESSO: A Modular and Open-Source Software Project for Quantum Simulations of Materials. *J. Phys. Condens. Matter* **2009**, *21*, 395502. [CrossRef]
47. Giannozzi, P.; Andreussi, O.; Brumme, T.; Bunau, O.; Buongiorno Nardelli, M.; Calandra, M.; Car, R.; Cavazzoni, C.; Ceresoli, D.; Cococcioni, M.; et al. Advanced Capabilities for Materials Modelling with Quantum ESPRESSO. *J. Phys. Condens. Matter* **2017**, *29*, 465901. [CrossRef]
48. Giannozzi, P.; Baseggio, O.; Bonfà, P.; Brunato, D.; Car, R.; Carnimeo, I.; Cavazzoni, C.; de Gironcoli, S.; Delugas, P.; Ferrari Ruffino, F.; et al. Quantum ESPRESSO toward the Exascale. *J. Chem. Phys.* **2020**, *152*, 154105. [CrossRef]
49. Abdelmoula, M.; Ruby, C.; Mallet, M.; Ghanbaja, J.; Coustel, R.; Scudiero, L.; Wang, W.-J. Identification of a $Fe(OH)_2$-like Phase in the Core–Shell Structure of Nano-Zero-Valent Fe and Its Evolution When Interacting with $Pd^{2+}{}_{aq}$ Ions by Mössbauer Spectroscopy, XPS, and TEM. *J. Phys. Chem. Solids* **2023**, *172*, 111066. [CrossRef]
50. Ramer, N.J.; Rappe, A.M. Designed Nonlocal Pseudopotentials for Enhanced Transferability. *Phys. Rev. B* **1999**, *59*, 12471–12478. [CrossRef]
51. Perdew, J.P.; Burke, K.; Ernzerhof, M. Generalized Gradient Approximation Made Simple. *Phys. Rev. Lett.* **1996**, *77*, 3865–3868. [CrossRef] [PubMed]
52. Monkhorst, H.J.; Pack, J.D. Special Points for Brillouin-Zone Integrations. *Phys. Rev. B* **1976**, *13*, 5188–5192. [CrossRef]
53. Benyelloul, K.; Bouhadda, Y.; Seddik, L.; Ghobrini, D.; Khodja, K. A First-Principle Study on Structural, Elastic Properties of Cubic and Tetragonal Mg_2CoH_5 Magnesium Complex Hydrides Under Pressure. In *Technological and Innovative Progress in Renewable Energy Systems*; Guerri, O., Arab, A.H., Imessad, K., Eds.; Advances in Science, Technology & Innovation; Springer: Cham, Switzerland, 2025; pp. 253–257. [CrossRef]

54. Wang, S.; Chen, L.; Hao, H.; Qiao, C.; Song, J.; Cui, C.; Liu, B. Study on the Infrared and Raman Spectra of Ti_3AlB_2, Zr_3AlB_2, Hf_3AlB_2, and Ta_3AlB_2 by First-Principles Calculations. *Sci. Rep.* **2024**, *14*, 15030. [CrossRef] [PubMed]
55. Zhang, J.; Cuevas, F.; Zaïdi, W.; Bonnet, J.-P.; Aymard, L.; Bobet, J.-L.; Latroche, M. Highlighting of a Single Reaction Path during Reactive Ball Milling of Mg and TM by Quantitative H_2 Gas Sorption Analysis to Form Ternary Complex Hydrides (TM = Fe, Co, Ni). *J. Phys. Chem. C* **2011**, *115*, 4971–4979. [CrossRef]
56. Cao, R.; Xu, Q.W.; Zhu, H.X.; Mao, G.J.; Lin, Q.; Chen, J.H.; Wang, P.-C. Weldability and Distortion of Mg AZ31-to-Galvanized Steel SPOT Plug Welding Joint by Cold Metal Transfer Method. *J. Manuf. Sci. Eng.* **2017**, *139*, 021001. [CrossRef]
57. $MgCo_2$ Crystal Structure. In *Inorganic Solid Phases*; Villars, P., Ed.; Springer: Berlin/Heidelberg, Germany, 2023. Available online: https://materials.springer.com/isp/crystallographic/docs/sd_1214030 (accessed on 14 April 2026).
58. Norek, M.; Nielsen, T.K.; Polanski, M.; Kunce, I.; Płociński, T.; Jaroszewicz, L.R.; Cerenius, Y.; Jensen, T.R.; Bystrzycki, J. Synthesis and Decomposition Mechanisms of Ternary Mg_2CoH_5 Studied Using in Situ Synchrotron X-Ray Diffraction. *Int. J. Hydrogen Energy* **2011**, *36*, 10760–10770. [CrossRef]
59. Didisheim, J.J.; Zolliker, P.; Yvon, K.; Fischer, P.; Schefer, J.; Gubelmann, M.; Williams, A.F. Dimagnesium Iron(II) Hydride, Mg_2FeH_6, Containing Octahedral FeH_6^{4-} Anions. *Inorg. Chem.* **1984**, *23*, 1953–1957. [CrossRef]
60. Bashir, A.I.; Arif, H.; Azam, S.; Irfan, M.; Khan, N. First-Principles Quantum Computations to Investigate Prospects of Mg_2FeH_6 for Optoelectronics and Hydrogen-Storage Applications. *Int. J. Hydrogen Energy* **2023**, *48*, 23930–23942. [CrossRef]
61. Parker, S.F.; Williams, K.P.J.; Smith, T.; Bortz, M.; Bertheville, B.; Yvon, K. Vibrational Spectroscopy of Tetrahedral Ternary Metal Hydrides: Mg_2NiH_4, Rb_3ZnH_5 and Their Deuterides. *Phys. Chem. Chem. Phys.* **2002**, *4*, 1732–1737. [CrossRef]
62. Parker, S.F.; Jayasooriya, U.A.; Sprunt, J.C.; Bortz, M.; Yvon, K. Inelastic Neutron Scattering, IR and Raman Spectroscopic Studies of Mg_2CoH_5 and Mg_2CoD_5. *J. Chem. Soc. Faraday Trans.* **1998**, *94*, 2595–2599. [CrossRef]
63. Wang, H.; He, Q.; Yang, Y. High-entropy Intermetallics: From Alloy Design to Structural and Functional Properties. *Rare Met.* **2022**, *41*, 1989–2001. [CrossRef]
64. Parker, S.F.; Williams, K.P.J.; Bortz, M.; Yvon, K. Inelastic Neutron Scattering, Infrared, and Raman Spectroscopic Studies of Mg_2FeH_6 and Mg_2FeD_6. *Inorg. Chem.* **1997**, *36*, 5218–5221. [CrossRef]
65. Zeng, X.Q.; Cheng, L.F.; Zou, J.X.; Ding, W.J.; Tian, H.Y.; Buckley, C. Influence of 3d Transition Metals on the Stability and Electronic Structure of MgH_2. *J. Appl. Phys.* **2012**, *111*, 093720. [CrossRef]
66. Xu, J.; Xu, Y.; Wang, L.; Guo, S.; Zhang, W.; Liu, J.; Li, B.; Sun, H.; Qi, Y.; Zhang, Y.; et al. Affected Hydrogen Storage Properties and Phase Transformation Characteristics of RE-Mg-Ni-Based Alloys by Adding Co. *J. Alloys Compd.* **2025**, *1042*, 183736. [CrossRef]
67. Verbovytskyy, Y.; Zhang, J.; Cuevas, F.; Paul-Boncour, V.; Zavaliy, I. Synthesis and Properties of the $Mg_2Ni_{0.5}Co_{0.5}H_{4.4}$ Hydride. *J. Alloys Compd.* **2015**, *645*, S408–S411. [CrossRef]
68. Wang, L.; Zhang, L.; Lu, X.; Wu, F.; Sun, X.; Zhao, H.; Li, Q. Surprising Cocktail Effect in High Entropy Alloys on Catalyzing Magnesium Hydride for Solid-State Hydrogen Storage. *Chem. Eng. J.* **2023**, *465*, 142766. [CrossRef]
69. Tran, X.Q.; McDonald, S.D.; Gu, Q.; Yamamoto, T.; Shigematsu, K.; Aso, K.; Tanaka, E.; Matsumura, S.; Nogita, K. In-Situ Investigation of the Hydrogen Release Mechanism in Bulk Mg_2NiH_4. *J. Power Sources* **2017**, *341*, 130–138. [CrossRef]
70. Čermák, J.; Král, L.; David, B. Hydrogen Diffusion in Mg_2NiH_4 Intermetallic Compound. *Intermetallics* **2008**, *16*, 508–517. [CrossRef]
71. Pericoli, E.; Barzotti, A.; Mazzaro, R.; Moury, R.; Cuevas, F.; Pasquini, L. Synthesis and Hydrogen Storage Properties of Mg-Based Complex Hydrides with Multiple Transition Metal Elements. *ACS Appl. Energy Mater.* **2025**, *8*, 4993–5003. [CrossRef]
72. Jiang, M.; Yang, Y.; Li, H.; Liang, B. Theoretical Study on the Surface Poisoning of High-Entropy Alloys during Hydrogen Storage Cycles: The Effect of Metal Elements and Phases. *Phys. Chem. Chem. Phys.* **2024**, *26*, 24384–24394. [CrossRef]
73. Zhou, P.; Bi, J.; Zhou, Q.; Lei, N.; Shen, H.; Jiang, J.; Song, D.; Xiao, X.; Chen, L. Unraveling the Contrasting Poisoning Mechanisms of AB_5- and AB_2-Type Hydrogen Storage Materials under Different Impurity Gases. *J. Energy Storage* **2026**, *141*, 119285. [CrossRef]
74. Chen, Y.; Zhou, P.; Bi, J.; Zhu, L.; Zhang, L.; Yan, C.; Jia, Y.; Xiao, X.; Wang, X.; Chen, L. Different Poisoning Behaviors of Impurity Gases on AB_2-Type Ti-Based Hydrogen Storage Alloys and Their Mechanisms. *J. Energy Chem.* **2026**, *114*, 350–361. [CrossRef]
75. Baraban, A.P.; Chernov, I.A.; Dmitriev, V.A.; Elets, D.I.; Gabis, I.E.; Kuznetsov, V.G.; Voyt, A.P. The Mg_2NiH_4 Film on Nickel Substrate: Synthesis, Properties and Kinetics of Formation. *Thin Solid Film.* **2022**, *762*, 139556. [CrossRef]
76. Albert, R.; Wagner, C.; Urbanczyk, R.; Felderhoff, M. Effective Thermal Conductivity of Dimagnesium Iron Hexahydride (Mg_2FeH_6) for Heat Storage Applications. *Appl. Phys. A* **2023**, *129*, 62. [CrossRef]
77. Baraban, A.P.; Dmitriev, V.A.; Gabis, I.E.; Voyt, A.P.; Klyamkin, S.N.; Shikin, I.V. Direct Synthesis of Mg_2NiH_4 from MgH_2 and Ni. *Phys. Complex Syst.* **2023**, *4*, 94–102. [CrossRef]
78. Khan, D.; Panda, S.; Ma, Z.; Ding, W.; Zou, J. Formation and Hydrogen Storage Behavior of Nanostructured Mg_2FeH_6 in a Compressed $2MgH_2$–Fe Composite. *Int. J. Hydrogen Energy* **2020**, *45*, 21676–21686. [CrossRef]
79. Assila, A.; Rkhis, M.; Alaoui-Belghiti, A.; Laasri, S.; Hlil, E.K.; Boughaleb, Y.; Hajjaji, A. Feeling the Strain: Enhancing the Thermodynamics Characteristics of Magnesium Nickel Hydride Mg_2NiH_4 for Hydrogen Storage Applications through Strain Engineering. *Int. J. Hydrogen Energy* **2024**, *67*, 651–657. [CrossRef]

80. Van Lai, D.; Nguyen, S.H.; Nguyen, A.H.; Van Nguyen, T.; Dinh, L.C.; Doan, P.D.; Pham, T.T.; Phung, V.H.T.; Tonezzer, M.; La, D.D.; et al. Tailoring Hydrogen Storage Performance of Mg-Mg_2Ni Alloys: Synergistic Effects of Composition and Phase Formation with First-Principles Insights. *RSC Adv.* **2025**, *15*, 31240–31254. [CrossRef]
81. Fadonougbo, J.O.; Kim, H.-J.; Suh, B.-C.; Yim, C.D.; Na, T.-W.; Park, H.-K.; Suh, J.-Y. On the Long-Term Cyclic Stability of near-Eutectic Mg–Mg2Ni Alloys. *Int. J. Hydrogen Energy* **2022**, *47*, 3939–3947. [CrossRef]
82. Puszkiel, J.A.; Arneodo Larochette, P.; Baruj, A.; Meyer, G.; Gennari, F.C. Hydrogen Cycling Properties of xMg–Fe Materials (x: 2, 3 and 15) Produced by Reactive Ball Milling. *Int. J. Hydrogen Energy* **2016**, *41*, 1688–1698. [CrossRef]
83. Kwon, Y.-S.; Gerasimov, K.B.; Yoon, S.-K. Ball Temperatures during Mechanical Alloying in Planetary Mills. *J. Alloys Compd.* **2002**, *346*, 276–281. [CrossRef]
84. Figueiredo, R.B.; Pereira, P.H.R.; Aguilar, M.T.P.; Cetlin, P.R.; Langdon, T.G. Using Finite Element Modeling to Examine the Temperature Distribution in Quasi-Constrained High-Pressure Torsion. *Acta Mater.* **2012**, *60*, 3190–3198. [CrossRef]
85. Sünbül, S.E.; İçin, K.; Aydoğdu, H.M.; Öztürk, S. The Production of Binary Mg-Ni Alloys and Ternary Mg-Ni-Based Alloys: The Structural and Corrosion Properties. *J. Alloys Compd.* **2025**, *1011*, 178463. [CrossRef]
86. Jung, S.J.; Sohn, S.S.; Lee, D.H.; Ko, W.-S.; Ha, T.J.; Kwak, R.-H.; Suh, B.-C.; Kim, Y.M.; Park, H.-K. Study on the Correlation between Microstructural Evolution and Hydrogen Storage Properties in Hyper-Eutectic Mg-xNi (x = 15, 20, 25) Alloys. *J. Mater. Res. Technol.* **2025**, *35*, 2068–2074. [CrossRef]
87. Edalati, K.; Akiba, E.; Horita, Z. High-Pressure Torsion for New Hydrogen Storage Materials. *Sci. Technol. Adv. Mater.* **2018**, *19*, 185–193. [CrossRef]
88. Révész, Á.; Gajdics, M.; Spassov, T. Microstructural Evolution of Ball-Milled Mg–Ni Powder during Hydrogen Sorption. *Int. J. Hydrogen Energy* **2013**, *38*, 8342–8349. [CrossRef]
89. Gajdics, M.; Calizzi, M.; Pasquini, L.; Schafler, E.; Révész, Á. Characterization of a Nanocrystalline Mg–Ni Alloy Processed by High-Pressure Torsion during Hydrogenation and Dehydrogenation. *Int. J. Hydrogen Energy* **2016**, *41*, 9803–9809. [CrossRef]
90. Vaidya, M.; Pradeep, K.G.; Murty, B.S.; Wilde, G.; Divinski, S.V. Radioactive Isotopes Reveal a Non Sluggish Kinetics of Grain Boundary Diffusion in High Entropy Alloys. *Sci. Rep.* **2017**, *7*, 12293. [CrossRef]
91. Ostovari Moghaddam, A.; Fereidonnejad, R.; Cabot, A. Semi-Ordered High Entropy Materials: The Case of High Entropy Intermetallic Compounds. *J. Alloys Compd.* **2023**, *960*, 170802. [CrossRef]
92. Yartys, V.A.; Lototskyy, M.V. Laves Type Intermetallic Compounds as Hydrogen Storage Materials: A Review. *J. Alloys Compd.* **2022**, *916*, 165219. [CrossRef]
93. Liu, J.; Wang, X.; Singh, A.; Xu, H.; Kong, F.; Yang, F. The Evolution of Intermetallic Compounds in High-Entropy Alloys: From the Secondary Phase to the Main Phase. *Metals* **2021**, *11*, 2054. [CrossRef]